Measurements of thermal properties of icy Mars regolith analogs

Matthew Siegler,[1,2] Oded Aharonson,[2] Elizabeth Carey,[2] Mathieu Choukroun,[3] Troy Hudson,[3] Norbert Schorghofer,[4] and Steven Xu[2,5]

Received 18 August 2011; revised 20 December 2011; accepted 20 December 2011; published 7 March 2012.

[1] In a series of laboratory experiments, we measure thermal diffusivity, thermal conductivity, and heat capacity of icy regolith created by vapor deposition of water below its triple point and in a low pressure atmosphere. We find that an ice-regolith mixture prepared in this manner, which may be common on Mars, and potentially also present on the Moon, Mercury, comets and other bodies, has a thermal conductivity that increases approximately linearly with ice content. This trend differs substantially from thermal property models based of preferential formation of ice at grain contacts previously applied to both terrestrial and non-terrestrial subsurface ice. We describe the observed microphysical structure of ice responsible for these thermal properties, which displaces interstitial gases, traps bubbles, exhibits anisotropic growth, and bridges non-neighboring grains. We also consider the applicability of these measurements to subsurface ice on Mars and other solar system bodies.

Citation: Siegler, M., O. Aharonson, E. Carey, M. Choukroun, T. Hudson, N. Schorghofer, and S. Xu (2012), Measurements of thermal properties of icy Mars regolith analogs, *J. Geophys. Res.*, *117*, E03001, doi:10.1029/2011JE003938.

1. Introduction

[2] Thermal properties of icy regolith are an important component in modeling and measuring the migration and presence of volatile-rich subsurfaces of rocky bodies throughout the Solar System. Thermal properties of icy regolith are also vital in quantifying surface and subsurface volatile content in remote sensing observations (namely infrared and microwave). Measurements of thermal properties of terrestrial icy soils have been made [e.g., *Kersten*, 1949; *Lachenbruch et al.*, 1982], but ice formation mechanisms are generally unknown. Numerous models of thermal properties of terrestrial icy soils have been developed [e.g., *Johansen*, 1975; *Farouki*, 1981; *Lachenbruch et al.*, 1982], but need to be extrapolated to extraterrestrial and extreme terrestrial conditions. Terrestrial icy soils typically experience periods in which migration of water in the liquid phase occurs, which can occur as thin films even at subfreezing temperatures [*Putkonen*, 2003; *Zent*, 2008].

[3] On Mars, the Moon, Mercury, comets, and other bodies with no atmospheres or atmospheric vapor pressures below the triple point, water is not long present in a liquid state. In these environments, H_2O and other volatiles migrate through the regolith by vapor diffusion, forming pore-filling structures that have been proposed to differ greatly from terrestrial soils [*Kossacki et al.*, 1994; *Mellon et al.*, 1997; *Piqueux and Christensen*, 2009b]. *Hudson et al.* [2009] constructed an experiment designed to produce icy soil from atmospheric vapor deposition of water under Martian pressure (6 mbar) and sub-freezing conditions. Here, we report the results of a series of thermal property measurements performed with this unique experimental setup at the Caltech Mars and Ice Simulations Laboratory.

[4] Thermal conductivity of ice-free, porous materials are reviewed by *Schotte* [1960], *Dul'nev and Sigalova* [1967], *Wechsler et al.* [1972], *Jakosky* [1986], *Tsotsas and Martin* [1987], *Presley and Christensen* [1997a], and *Carson et al.* [2005]. Measurements of dry particulate thermal conductivity have been conducted for industrial applications [e.g., *Smoluchowski*, 1910], and in association with the Apollo lunar program [e.g., *Wechsler and Glaser*, 1965; *Fountain and West*, 1970; *Cremers*, 1971; *Cremers and Hsia*, 1974]. More recent experiments have been carried out in a CO_2 atmosphere in the Martian atmospheric pressure regime [*Presley and Christensen*, 1997b; *Presley and Craddock*, 2006; *Presley and Christensen*, 2010].

[5] Past experiments lead to several conclusions, the foremost being that at low atmospheric pressures (and low temperatures) the small physical contacts between grains limit heat conduction through the medium and lead to extremely low bulk thermal conductivity and thermal diffusivity. This is demonstrated on the lunar surface where vacuum conditions cause thermal conductivities below 10^{-3} W m^{-1}K^{-1} [*Langseth et al.*, 1976; *Vasavada et al.*, 1999]. Similarly, dry regolith on the Martian surface, with only ~6 mbar total atmospheric pressure, can also have extremely low thermal conductivities ranging from roughly

[1]Department of Earth and Space Sciences, University of California, Los Angeles, California, USA.
[2]Division of Geologic and Planetary Sciences, California Institute of Technology, Pasadena, California, USA.
[3]Jet Propulsion Laboratory, California Institute of Technology, Pasadena, California, USA.
[4]Institute for Astronomy, University of Hawaii, Honolulu, Hawaii, USA.
[5]Department of Astronautical Engineering, University of Southern California, Los Angeles, California, USA.

0148-0227/12/2011JE003938

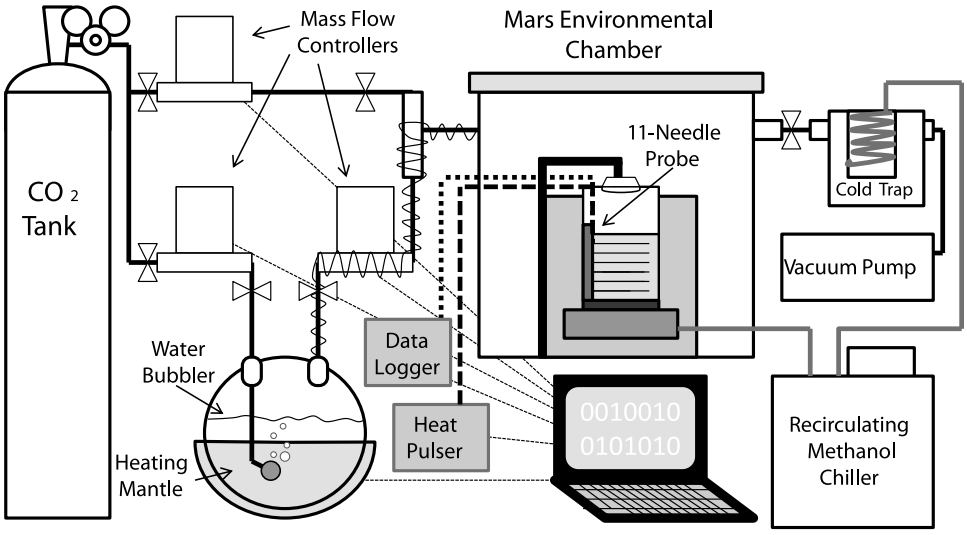

Figure 1. Schematic of experimental setup. The chamber maintains a 6 mbar CO_2 atmosphere with water vapor content regulated by several mass flow controllers. The sample is chilled from below by liquid methanol and heated at the surface by a small halogen lamp. A detail of the probe is seen in Figure 2.

0.02 to 0.1 W $m^{-1}K^{-1}$ [*Presley and Christensen*, 1997b; *Putzig and Mellon*, 2007]. However, deposition of even small amounts of ice or cement placed at grain contacts can potentially increase the conductivity dramatically and has been proposed to dominate thermal properties even if present in small quantities [*Mellon et al.*, 1997; *Piqueux and Christensen*, 2009b; *Wood*, 2011]. In this paper, we will experimentally examine how pore-filling structures affect thermal properties when delivered by a condensing vapor.

[6] To define the properties measured here, the heat flux in one dimension is given by $-\lambda\partial T/\partial z$, with thermal conductivity, λ, defined as a proportionality factor between the heat flux and the temperature gradient, $\partial T/\partial z$. The one-dimensional heat equation is

$$\rho c\frac{\partial T}{\partial t}=\frac{\partial}{\partial z}\left(\lambda\frac{\partial T}{\partial z}\right) \tag{1}$$

where ρ is the bulk density and c is the heat capacity. If the thermal properties are constant in space then

$$\frac{\partial T}{\partial t}=\frac{\lambda}{\rho c}\frac{\partial^2 T}{\partial z^2}=\kappa\frac{\partial^2 T}{\partial z^2} \tag{2}$$

where thermal diffusivity is defined by $\kappa = \lambda/(\rho c)$. Our objective is to measure thermal diffusivity, κ, conductivity, λ, and the volumetric heat capacity, ρc as a function of ice content. Another combination of these parameters, $I = \sqrt{\lambda\rho c}$, is known as thermal inertia and can also be calculated from our measurements. This quantity is of special relevance because it can be determined by remote sensing of time varying surface temperatures [*Christensen and Moore*, 1992; *Putzig and Mellon*, 2007].

[7] Several models for thermal conductivity of ice-filled and cemented regolith in Martian environments have been proposed [*Mellon et al.*, 1997; *Schorghofer and Aharonson*, 2005; *Piqueux and Christensen*, 2009b]. However, these models have not been tested experimentally under Martian analog conditions. Here we examine a series of measurements of thermal properties of icy regolith simulant filled by vapor diffusion at subfreezing temperatures under Martian atmospheric pressure. These experiments are pertinent to thermal properties of icy regolith assumed to have formed by vapor transport on Mars, but also may be applicable for a variety of solar system bodies, including the shallow subsurfaces of Earth, the Moon, Mercury, icy asteroids, comets, and other bodies.

2. Experimental Setup and Methods

2.1. Experimental Apparatus

[8] The experiments described here measure thermal properties of icy regolith created from direct deposition of atmospheric water vapor under Martian surface conditions. A specially designed thermal properties probe was imbedded in the vapor diffusion experiment to monitor changes in thermal conductivity, diffusivity, and volumetric heat capacity with ice growth.

[9] The experimental setup is similar to that described in detail by *Hudson et al.* [2009] and *Hudson* [2009] and consists of a small (30 cm diameter, 40 cm high, cylindrical) environmental chamber with controlled temperature, humidity, and pressure. Figure 1 illustrates this setup. The chamber is filled with a steady flow-through of CO_2 maintained at 6 mbar to simulate average Mars surface conditions. Within this chamber, a small regolith stimulant sample, generally 500–600 μm diameter glass spheres, Jaygo Dragonite, as given by *Presley and Christensen* [1997b] sits in a 7.5 cm acrylic cylinder with a removable, 1 cm-thick, brass base. Temperatures are controlled at the surface of the sample (to 266 $\pm$ 1.2 K) and the brass plate at the bottom of the sample is cooled by a recirculating methanol chiller. The temperature of the bottom of the soil sample is typically 212 K with up to a 5 K variation between experiments. This results in an average gradient of $\sim$9–11 K cm^{-1} through the 5 cm tall sample. Surface temperature was controlled by a PID loop which takes in measurements from a small T-type thermocouple placed on the sample surface within a few mm of the

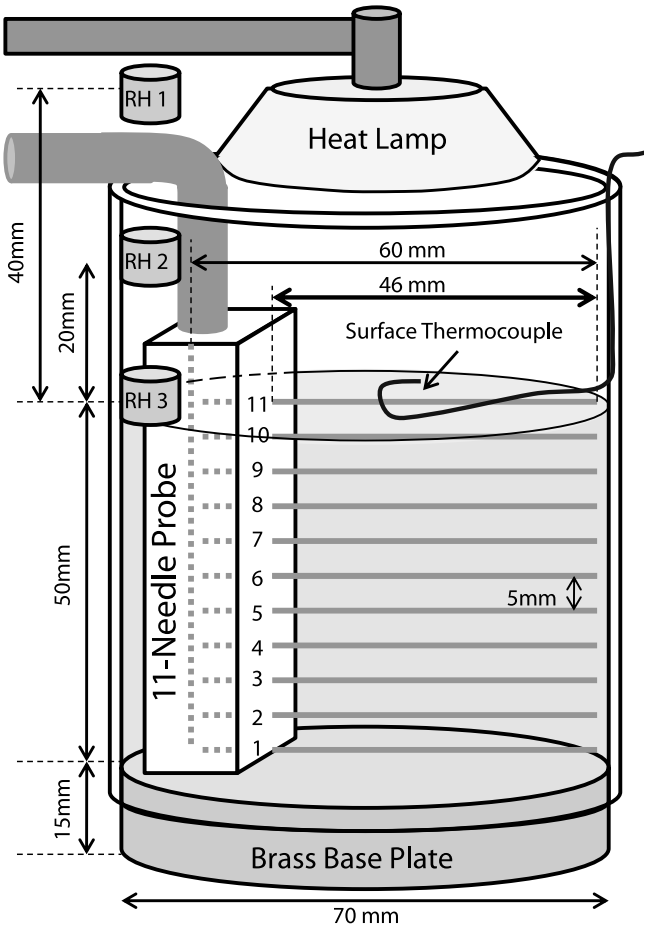

Figure 2. Schematic illustration of 11-needle thermal properties probe. Each needle contains a heater and thermocouple. The brass base plate is in contact with a cold plate chilled by liquid methanol, the surface is heated by the lamp.

top probe needle. A LabView controller then outputs a proportional voltage through an amplifier to a frosted halogen lamp sitting about 5 cm above the sample surface.

[10] After reaching thermal equilibrium, water vapor is mixed into the CO_2 supply and released into the environmental chamber. When water vapor is introduced, the thermal gradient results in a strong saturation vapor density gradient which drives water molecules down into the medium [*Mellon and Jakosky*, 1993; *Hudson et al.*, 2009]. The surface temperature, total atmospheric pressure, and water vapor pressure are all independently controlled by several PID (Proportional-Integral-Derivative) control loops run through LabView software.

[11] The water vapor density is controlled by a PID loop according to measurements from one of three small relative humidity sensors affixed inside the sample cup: one at the sample surface, one at 2 cm above the sample surface, and one just above the top edge of the sample cup (about 4 cm above the sample surface). Each of these RH/RTD (Relative Humidity/Resistance Temperature Device, Honeywell model HIH-4602-C) sensors is calibrated to convert relative humidity to partial pressure of water [*Hardy*, 1998]. Vapor density is calculated assuming the ideal gas law with the measured RTD temperature. Using a 6 mbar total atmospheric pressure and 1.6 g cm^{-3} water vapor density at the sample surface, the water vapor reaches saturation at a 6–10 mm depth in the sample (where temperatures are about ~268 K), and typically forms a sharp ice table in this region with decreasing ice content below [*Hudson et al.*, 2009]. Therefore, any given experiment produces a range of ice contents (reported as pore filling fractions) as a function of depth. The rate of ice deposition slows down exponentially with time throughout the experiments due to pore space constriction, from a maximum of 2 kg m^{-3} s^{-1} to less than 0.2 kg m^{-3} s^{-1} over the course of a several week experiment [*Hudson et al.*, 2009].

[12] Ice content is measured gravimetrically after completion of an experiment. To accomplish this, the column of icy soil was pushed out of the sample cup by using the bottom brass plate as a piston, then sliced into 5 mm thick sections. These sections were weighed before and after baking them for >24 h in a 130°C oven. Experiments presented here use a multineedle, line source heat-pulse method [*Campbell et al.*, 1991; *Bristow et al.*, 1994], allowing for in situ measurement of thermal conductivity, thermal diffusivity, and specific heat capacity. In this method, a single linear heater is briefly activated and then its cooling is monitored to determine thermal conductivity of the surrounding medium. The flow of heat to a neighboring, unheated needle is also monitored to extract thermal diffusivity and heat capacity. The heat pulse is of short enough duration (~10 s) that it is assumed to have little effect on ice deposition in the medium. A probe with 11 horizontal needles remained in the sample medium during the experiment (Figure 2).

[13] The 11 needles, each 60 mm long and 1 mm in diameter, have an internal resistor of 1000 Ω m^{-1} running the length of the needle (Evanohm, custom constructed by East 30 Sensors) and were typically pulsed with a constant voltage of 6 ± 0.01 V (outputting a total of 10.9 W m^{-1}). The entire heat pulse is assumed delivered to the soil in our analysis. However, very low thermal conductivity measurements may be slightly affected by contact resistance between the needles and the beads. With contact resistance, a fraction of the heat flows into the body of the probe instead of the sample. To decrease the chance of heat flow into the probe, the body was constructed of low thermal conductivity epoxy in a Teflon spine with the needles at 5 ± 0.2 mm vertical spacing. The spine itself is a 15 mm × 15 mm × 70 mm hollowed channel with 11 holes. The needles each protruded about 46 mm from these holes and have an internal, E-type thermocouple at the center of the exposed portion of the needle, 23 mm from the end. The probe is constructed partially at 30-East Sensors and partially at Caltech. About 2 mm of beads lay between the needle tips and the far wall of the sample cup, limiting conduction to the facing wall. The needle thermocouples are calibrated against a reference T-type thermocouple in 0°C ice bath to correct for fluctuations within our data logger units (two Measurement Computing USB-TCs).

[14] The heater, RH/RTD, lamp, and thermocouple wires from the probe feed through the chamber wall individually and their measurement is digitized by National Instruments (DAQ-9172) and Measurement Computing (USB-1608FS and USB-TC) data loggers. Chamber temperature and pressure is controlled at approximately 3 s intervals while data

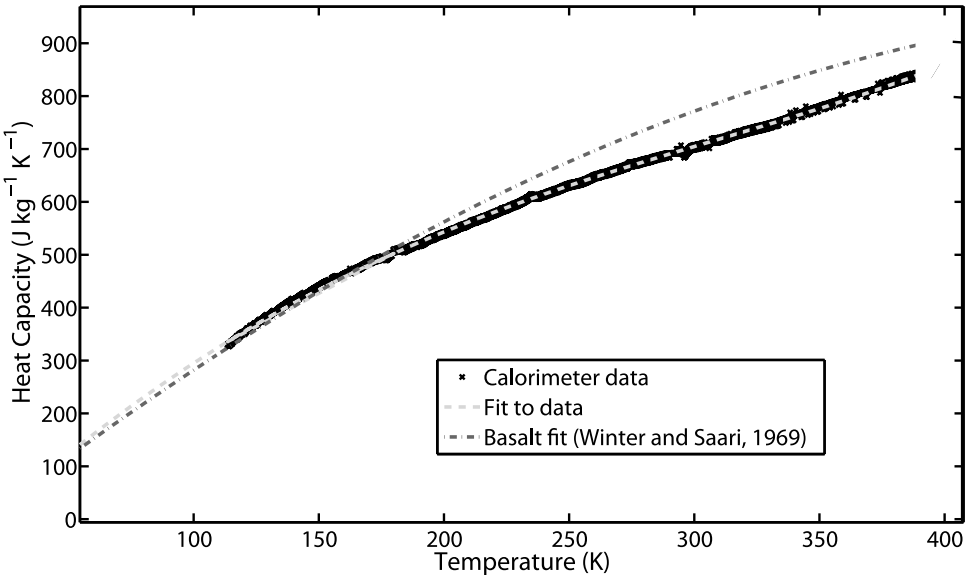

Figure 3. Measurement of specific heat capacity, c, and a 3rd-order fit (equation (3)) as compared to a fit to basaltic materials (equation (4)) [*Winter and Saari*, 1969, equation 16].

from the needle thermocouples and heaters is recorded and time-stamped once per second.

2.2. Regolith Simulants

[15] The ice filling experiment described here uses a bed of loosely packed (~43% porosity) glass spheres sieved to between 500 μm to 600 μm in diameter. The relatively large grain size was chosen to allow for fast vapor diffusion, the spherical shape for ease of void space estimation and theoretical modeling. The beads were chosen for their regular shape (see section 6) and to replicate the study of *Presley and Christensen* [1997b]. Before each experiment, the beads were washed in deionized water, resieved, and baked at >130°C for at least one day.

[16] The beads are approximately 72% SiO_2, 14% Na_2O, and 9% CaO and should not have any strong surface water adsorption properties (Jaygo Dragonite™ technical data sheet). This glass mixture has a solid density of about 2750 kg m^{-3} and a solid thermal conductivity of about $(1.5 \times 10^{-3}$ (T-273) + 1.1277) W m^{-1} K^{-1} (for temperature T in K, fit from Sciglass™ database).

[17] We used a Setaram BT2.15 cryogenic calorimeter to measure the heat capacity of the glass beads. This LN2-cooled calorimeter is equipped with a sample and a reference cell, which are housed inside the calorimetric block. Calvet elements (three-dimensional arrays of 64 thermocouples) are used to measure the heat flux to the cells with a precision of 0.1 μW and use the reference cell as a differential, providing a direct measurement of the heat flux solely affecting the sample. Heat capacity is derived from the ratio of the heat flux delivered to the sample to sample mass as a function of imposed heating rate.

[18] The experimental results are plotted in Figure 3 and were conducted on a 12.1 g sample of glass beads heated at a rate of 0.2 K min^{-1} from 110 to 400 K. These results show a significant discrepancy (~10% above 200 K) from the fit to basalt samples presented by *Winter and Saari* [1969]. Parameters for equation (3) have been derived by nonlinear regression of our calorimeter data resulted in:

$$c_{dry} \approx (1.28 \times 10^{-5} T^3 - 1.19 \times 10^{-2} T^2 + 5.14\mathrm{T} - 110.4)\ \mathrm{J\ kg^{-1}K^{-1}} \quad (3)$$

valid between about 110 and 395 K. Equation (3) is used to calculate c_{dry} of our glass beads throughout this paper.

[19] Further measurements were conducted with JSC Mars-1 Regolith simulant [*Allen et al.*, 1998; *Seiferlin et al.*, 2008]. Though this simulant is designed as a spectral analog for Mars, it can add confidence to the relevance of the glass bead thermal measurements to real Martian regolith which is likely to have basaltic composition and irregular shape. For comparison with glass bead measurements, the JSC Mars-1 was also sieved between 500 and 600 μm and dried in a similar manner. The sifted 500–600 μm JSC Mars-1 had a measured a bulk density of 0.66 ± 0.05 g cm^{-3} with an assumed particle density of 1.91 g cm^{-3} [*Allen et al.*, 1998], resulting in a 65% porosity. We assign a 10% uncertainty of our sieved JSC Mars-1solid particle density as we may have removed either a lighter or denser component. The solid conductivity of this basalt is expected to be approximately 2 W m^{-1} K^{-1} [*Langseth et al.*, 1976] and was not modeled to vary with temperature. This thermal conductivity should be nearly twice that of the glass spheres, which will be revisited in section 5.5. The specific heat capacity represented by equation (4) is based on past work applicable to basalt minerals and used in this paper to best represent JSC Mars-1 [*Winter and Saari*, 1969],

$$c_{dry\,basalt} \approx (-34\ T^{1/2} + 8\ T - 0.2\ T^{3/2})\ \mathrm{J\ kg^{-1}K^{-1}}. \quad (4)$$

As the beads are made of silica glass and were washed in deionized water, their surfaces may be hydrophobic relative to JSC Mars-1 and other natural samples.

Table 1. Experimental Runs

Description or Filling Duration	Volumetric Filling Range, F (%)	Total Pressure P, (mbar)
7 h	0–7.9	6
11 h	2.6–9.9	6
24 h	4.4–16.1	6
25.7 h	8.9–26.5	6
48.6 h	18.3–34.8	6
98 h	23.1–50.1	6
220 h	41.8–69.9	6
570 h	57.3–75.5	6
Dry	0	1–12
Saturated beads	~100	6
JSC Mars-1 269 hour	62.5–82.5	6
Saturated JSC Mars-1	~100	6
Pure ice	N/A	6

2.3. Experimental Procedure

[20] A set of vapor deposition experiments were performed under roughly identical conditions and stopped at various durations in order to span a range of ice contents. Table 1 presents a list of the experimental runs between 0 and 570 h in length and the pore filling fractions achieved as well as several non-vapor deposited experiments.

[21] Prior to each experiment roughly 280 g sample of 500–600 μm glass beads were baked in a 130°C oven for at least 24 h and cooled, then poured into the sample cup, to form a 5 cm deep layer around the 11-needle probe. The bottom of the brass base of the sample cup is coated with a thin layer of silicon heat transfer compound, and then placed upon a cooling plate through which an external Neslab ULT 95 chiller recirculates methanol at ~−90°C.

[22] The chamber is sealed, and then pumped down to roughly 1 mbar for at least 8 h at room temperature prior to cooling the sample (which takes another 6–12 h to reach thermal equilibrium). Absolute atmospheric pressure is then controlled by a second PID loop to 6 ± 0.2 mbar for the duration of the experiment. The PID loop controls a throttled bleed-in of dry or wet CO_2 and a rough vacuum pump draws excess gas from the chamber. A small LACO cold trap (also cooled by the methanol chiller) collects water vapor in the vacuum line. Once all the thermocouple temperatures are stable to within 0.1 K hr^{-1} the experiment is assumed in thermal equilibrium and a controlled flow CO_2 and water vapor is allowed into the chamber (time zero in the quoted experiment duration; see Table 1). During the experiment, water vapor density is controlled with a third PID loop (at 1.6 g cm^{-3} in the presented experiments) as measured by the RH/RTD at the sample surface. Total atmospheric pressure is maintained at 6 ± 0.2 mbar after the water vapor flow begins.

[23] To measure thermal properties in situ, the 11 needles of the probe are pulsed (out of order 1,7,2,8…, index increasing upward, to provide the largest distance between consecutive pulses) with 6 V for 10 s each. The heat liberated per unit length per unit time, q' (usually 10.9 W m^{-1}), is determined within 5.5% from this input voltage and the heater specification. The uncertainty is mainly due to an unforeseen rise in resistance by ~3 ohms as needle wires aged, which is included as an error is our assumed q'. Pulses were kept to 10 s so that the top needle (not used in this analysis) did not exceed 0°C, and all others did not exceed −10°C as recommended by *Putkonen* [2003] who observed a dramatic change in thermal properties above this temperature, presumably due to thin films. Five minutes are given between pulses to allow the heat to fully dissipate. We required at least three minutes of data after each pulse in fits of heat pulses from a neighboring needle.

[24] The experiment is then run in a stable environment for a period of a few hours to nearly a month. Thermal properties were measured at least once per hour at each depth. At the completion of an experiment the sample is covered with aluminum foil and moved to a −10°C cold room to be sampled as soon as possible. Within the cold room, the sample is sliced into 5 mm thick discs, and then weighed before and after a >24 h drying period in a 130°C oven [*Hudson*, 2009]. The mass loss between weighing corresponds to the ice content in each sample layer. The corresponding thermophysical properties of each layer are derived from final heat pulses (within the last hour before removal) of the needles adjacent to that layer.

3. Experimental Techniques

3.1. Line Source Heat-Pulse Method

[25] The 11-needle thermal probe utilizes both standard single and dual probe line source heat-pulse measurements. The single probe method [*De Vries*, 1952] uses a thin, epoxy-filled, hollow needle equipped with both an internal heater and thermocouple. When a brief pulse of electricity is applied to the needle, the heat produced will flow into the surrounding medium at a rate depending on the medium's thermal properties. A higher thermal conductivity medium will cause the needle to reach a lower maximum temperature during heating and to cool more rapidly once the pulse has ceased.

[26] *De Vries* [1952] developed a Green's function solution (similar to that detailed in section 3.2) for a radial, cylindrically symmetric heat pulse (length t_0) in which thermal conductivity, diffusivity, and volumetric heat capacity can be solved for assuming a homogeneous and isotropic medium:

$$\Delta T(r,t) = -\frac{q'}{4\pi\kappa\rho c} Ei\left(\frac{-r^2}{4\kappa t}\right) \text{ for } 0 < t \le t_0 \tag{5}$$

during the heat pulse, or

$$\Delta T(r,t) = \frac{q'}{4\pi\kappa\rho c}\left[Ei\left(\frac{-r^2}{4\kappa(t-t_0)}\right) - Ei\left(\frac{-r^2}{4\kappa t}\right)\right] \text{ for } t > t_o. \tag{6}$$

ΔT is the temperature change at a distance r from the source, q' the heat per unit length per unit time (generally ~10.9 W m^{-1}), and Ei is the Exponential Integral function $Ei(x) = \int_{-\infty}^{x} (e^s/s)\,ds$.

[27] Near the heat pulse source, r is small, and the Ei term is approximated by $Ei(x) \approx \gamma + \ln(-x)$, where γ is Euler's constant ≈0.5772. *Bristow et al.* [1994] denote the temperature offset with d and add an empirical time offset, t_c. Equation (5) becomes

$$\Delta T \approx \frac{q'}{4\pi\lambda}\ln(t + t_c) + d\, 0 < t \le t_0. \tag{7}$$

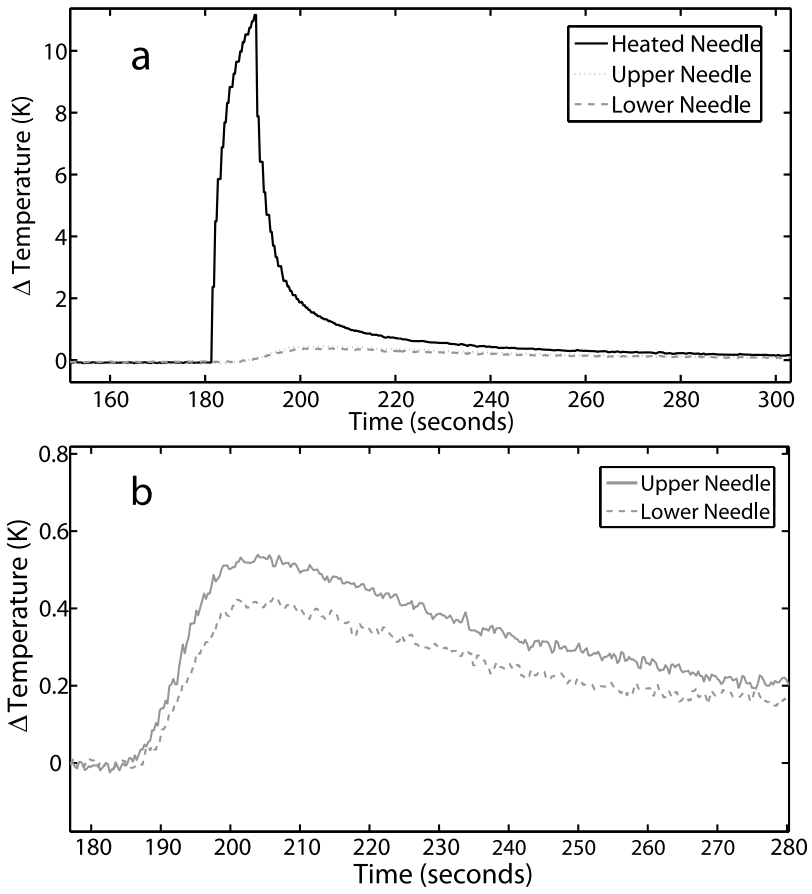

Figure 4. (a) Example of heated needle temperature changes in an isothermal, room temperature, ice free sample. The large, single needle pulse is fit by equation (7) before t_o and equation (8) after. The duration of the heat pulse was t_o = 10 s. (b) A detailed view of the neighboring needle temperatures, which are fit by equation (20) before t_o and equation (21) after.

In the same approximation, equation (6), the response after the pulse is complete, becomes

$$\Delta T \approx \frac{q'}{4\pi\lambda}[\ln(t+t_c) - \ln(t+t_c-t_o)] + d \text{ for } t > t_0. \quad (8)$$

[28] These quantities are solved for by a nonlinear regression to the data. A principal shortcoming of the single probe method is that it only results in a measurement of thermal conductivity, while thermal diffusivity and heat capacity of the medium remain unmeasured. This can be seen in equations (7) and (8) where the quantity $\kappa\rho c$ is rewritten as thermal conductivity, λ. These equations assume that the thermal conductivity is identical in all directions which, as discussed in section 3.2, may not necessarily be true. Another shortcoming is the susceptibility of this measurement technique to contact resistance for short timescales (<∼270 s, [*Cull*, 1978]), which can decrease the effective heat, q', released into the sample. This will increase the measured value of λ during heating (as heat is not allowed to escape the needle) and decrease the measured λ during cooling (as heat is not deposited into the medium). Example heating/cooling data is shown in Figure 4.

[29] In a dual-probe measurement one needle serves as a heat source and a neighboring needle serves as a temperature probe. Therefore a nonlinear, piecewise fit to equation (5) and (6) can be used. Our method for deriving thermal properties, which includes effects due to anisotropic heat flow, is discussed in section 3.2.

3.2. Line Source Heat-Pulse Method in Anisotropic Medium

[30] As ice may preferentially grow along a thermal gradient, we generalize the equations used for single and dual probe measurements of thermal conductivity to an anisotropic medium, where the conductivity in the vertical (z) direction may differ from that in a direction within the horizontal plane (x). The temperature and conductivity are assumed constant along the line source (y).

[31] Due to the strong thermal gradient in the sample heat will not only flow radially from each needle, but also vertically along the gradient. This requires a modification of the dual-probe fit. The gradient, dT/dz, defined as g, is assumed linear (see Appendix A). For our analysis, the term gz is obtained from the time-averaged measured temperature from the needle prior to a heat pulse.

[32] As first step, we seek the solution to the anisotropic, i.e., κ depends on direction, but spatially homogeneous, i.e., κ is independent of x and z, heat equation

$$\frac{\partial T}{\partial t} = \kappa_x \frac{\partial^2 T}{\partial x^2} + \kappa_z \frac{\partial^2 T}{\partial z^2}, \quad (9)$$

for an instantaneous heat pulse at time $t = 0$ and an initially linear temperature profile. Because anisotropy in conductivity is a result of preferential ice formation caused by the temperature gradient, z is aligned with a principal axis of the diffusivity. It is convenient to write the solution in terms of $\Delta T(x, z, t) = T(x, z, t) - gz$, where the linear term gz satisfies (9) and also represents the initial condition, $T(x, z, 0) = gz$. While $T(x, z, t)$ is the exact solution for an infinite domain, it also approximates the temperature distribution in the vicinity of the line source if the boundaries of the domain are far from the line source.

[33] Using standard methods for partial differential equations, this solution is obtained as

$$\Delta T(x,z,t) = \frac{q}{4\pi\rho c\sqrt{\kappa_x\kappa_z}t}\exp\left(-\frac{x^2}{4\kappa_x t}-\frac{z^2}{4\kappa_z t}\right), \tag{10}$$

where q is the heat per unit length. The line source is located at $(x, z) = (0, 0)$. It is easily verified that equation (10) satisfies the heat equation (9) and conserves the total amount of heat (again per unit length),

$$\rho c\int_{-\infty}^{+\infty}dx\int_{-\infty}^{+\infty}dz\Delta T(x,z,t) = q. \tag{11}$$

[34] It also satisfies the desired boundary condition, $\Delta T = 0$, infinitely far from the line source. Solution (10) is the Green's function of equation (9) for a source at $(x, z) = (0, 0)$. The solution for a prolonged, finite heat pulse (subscript f) is obtained by integration of the Green's function over time,

$$\Delta T_f(x,z,t) = \int_0^t dt'\Delta T(x,z,t-t') \tag{12}$$

$$= -\frac{q'}{4\pi\rho c\sqrt{\kappa_x\kappa_z}}Ei\left(-\frac{x^2}{4\kappa_x t}-\frac{z^2}{4\kappa_z t}\right)\text{ for } 0 < t \le t_0, \tag{13}$$

where Ei is again the Exponential Integral function and q' is the heat input per unit length per unit time. The solution for a heat pulse of finite duration, from $t = 0$ to $t = t_0$, is obtained by integration of the Green's function over that period,

$$\Delta T_f(x,z,t) = \int_0^{t_0} dt'\Delta T(x,z,t-t') \tag{14}$$

$$= \frac{q'}{4\pi\rho c\sqrt{\kappa_x\kappa_z}}\left[Ei\left(-\frac{x^2}{4\kappa_x(t-t_0)}-\frac{z^2}{4\kappa_z(t-t_0)}\right) - Ei\left(-\frac{x^2}{4\kappa_x t}-\frac{z^2}{4\kappa_z t}\right)\right]\text{ for } t > t_0. \tag{15}$$

Again, it can be verified that equations (13) and (15) satisfy (9) and, respectively,

$$\rho c\int_{-\infty}^{+\infty}dx\int_{-\infty}^{+\infty}dz\Delta T_f(x,z,t) = q't \quad \text{for } 0 < t \le t_0 \tag{16}$$

and

$$\rho c\int_{-\infty}^{+\infty}dx\int_{-\infty}^{+\infty}dz\Delta T_f(x,z,t) = q't_0 \quad \text{for } t > t_0. \tag{17}$$

[35] From equations (13) and (15) we obtain the relation needed to invert the single probe measurements for small x and z,

$$\Delta T_f = \frac{q'}{4\pi\rho c\sqrt{\kappa_x\kappa_z}}\ln(t) + d \quad \text{for } 0 < t \le t_0 \tag{18}$$

and

$$\Delta T_f = \frac{q'}{4\pi\rho c\sqrt{\kappa_x\kappa_z}}\ln\frac{t}{(t-t_0)} \quad \text{for } t > t_0. \tag{19}$$

This provides measurement of $\rho c\sqrt{\kappa_x\kappa_z} = \sqrt{\lambda_x\lambda_z}$, which is the geometrically averaged conductivity. The relevant equations for dual probe measurements are

$$\Delta T_f(0,z,t) = -\frac{q'}{4\pi\rho c\sqrt{\kappa_x\kappa_z}}Ei\left(-\frac{z^2}{4\kappa_z t}\right) \quad \text{for } 0 < t \le t_0 \tag{20}$$

and

$$\Delta T_f(0,z,t) = \frac{q'}{4\pi\rho c\sqrt{\kappa_x\kappa_z}}\left[Ei\left(-\frac{z^2}{4\kappa_z(t-t_0)}\right) - Ei\left(-\frac{z^2}{4\kappa_z t}\right)\right] \quad \text{for } t > t_0. \tag{21}$$

[36] The time and distance dependence provides measurement of κ_z; the prefactor combined with κ_z and q' provides $\rho c\sqrt{\kappa_x/\kappa_z}$. Only in the isotropic case does it provide a separate measurement of ρc. The measurement of $\rho c\sqrt{\kappa_x/\kappa_z}$ depends directly on knowledge of heat input, q', and thus is sensitive to any contact resistance and heat loss to the body of the probe. The thermal diffusivity, κ_z, is unaffected by errors in q', as it falls within the Exponent Integral in equations (20) and (21). Error analysis of the nonlinear fit to (20) and (21) is detailed in Appendix A.

3.3. Data Analysis Methods

[37] Heated needle data during the heat pulse are generally too coarse (only 10 data points at a collection rate of 1 per second) for a robust fit, so thermal conductivity (as derived from the single needle measurement) is obtained by a nonlinear fit of equation (8), to the cooling trend of the needle. The single-needle method inherently samples the entire medium around the needle and is not sensitive to possibly anisotropic heat flow (see section 3.2). This method is also more susceptible to resistance caused by poor contact between the needle and the surrounding medium [*Cull*, 1978], mimicking a change in thermal properties. Both of these errors directly effect the heat input to the sample, q' in equations (7) and (8), and are not separated here.

[38] The temperature change at a needle above and below a pulsed needle can be used to determine the thermal diffusivity of the medium between the needles. The temperature increase at the neighboring needle was less than 1 K (Figure 4b), so a sensitive thermocouple is necessary for a good fit (the E-type thermocouples here had a roughly

0.02 K error). A fit to the next farthest needle (10 mm away) proved impossible without exceeding 263 K at some needle.

[39] The effect of the thermal gradient was removed by subtracting a time averaged temperature of the sensing needle for the 100 s prior to the heat pulse. Then a nonlinear fit was computed to the temperature profile using equation (20) for times $t < t_o$ and equation (21) for $t \geq t_o$. This allows a separate estimate of κ_z and $\rho c\sqrt{\kappa_x/\kappa_z}$, or κ and ρc if the medium is isotropic. Needles 1 and 11 (top and bottom) were not used for the thermal properties analysis due to their proximity to the sample boundaries. The horizontal sample size is a factor of a few larger than the characteristic length scale for diffusion of heat (for typical diffusivities $<1 \times 10^{-6}$ m s^{-2}) during the ~3–5 min of data used for the fits, so edge effects are neglected.

[40] The derived thermal property values at each needle can then be directly associated with the gravimetrically measured ice fraction of the medium most closely represented by that needle. Ice content is measured at the end of a given experiment, so only conductivity values from the last hours (last pulse of each needle) from each experiment are presented here. These results may be used to estimate ice content in situ in the future.

[41] At the end of an experiment, the chamber is returned to room pressure and the sample container is immediately moved to the 263 K sampling room. The brass bottom of the sample is designed to be incrementally pushed up through the sample cup to allow thin layers to be either brushed or sawed (in the case of ice cemented soils) for gravimetric analysis. Horizontal slices of the sample, taken at 5 mm intervals, and all loose material are funneled into glass beakers and immediately weighed to give the total layer mass, m_t. Material may be sampled at this point for microscopic documentation (such material is not included in m_t, but is negligible compared to the total mass). The beakers are then baked at 390 K for at least 24 h, cooled, then weighted to obtain the dry sample mass, m_s.

[42] The ice content can be expressed as the pore filling fraction $F = \sigma/\sigma_0$, where σ is the ice density in the available volume, $\sigma = \rho_{bulk}(m_t/m_s - 1)$, and σ_0 is the maximum possible density of ice (filled pores), $\sigma_0 = \epsilon_0\rho_{ice}$. The bulk density of the dry medium, ρ_{bulk}, is 1570 ± 10 kg m^{-3} for glass beads and ρ_{ice} is taken as 918 kg m^{-3} [*Lide*, 2003].

4. Theoretical Expectations

4.1. Modes of Heat Transport in Porous Media

[43] The effective thermal conductivity of a porous medium is generally subdivided into three parallel heat paths: λ_{bs}, the conduction through the bulk solid (which includes grain to grain contact resistance), λ_g, the conduction via the pore space gas, and λ_r, the radiative conduction through the pore space [*Wechsler et al.*, 1972; *Jakosky*, 1986]. These same conceptual divisions apply to thermal diffusivity, but are discussed in terms of conductivity here for comparison with prior literature.

[44] In particulate media, grain contact points create a bottleneck for heat flow, and thus λ_{bs} can be very small. Therefore the thermal conductivity of solid rock (or ice), λ_s, can be orders of magnitude higher than λ_{bs} of the same material. λ_{bs} depends highly on grain size [*Presley and Christensen*, 1997b; *Slavin et al.*, 2002; *Piqueux and Christensen*, 2009a], grain roughness [*Bahrami et al.*, 2006], shape, and particle mixture (*Presley and Craddock* [2006], including cemented grains [*Presley and Christensen*, 2010; *Piqueux and Christensen*, 2009b]). At temperatures below those tested in our lab, λ_s may have a strong temperature dependence as phonon heat transfer within the solid grains is inhibited. Throughout this paper λ_{bs} is often combined with λ_g as λ_{dry}.

[45] *Presley and Christensen* [1997b] found the gas conductivity, λ_g, to have a $P^{0.6}$ dependence of conductivity when gases are confined in a fine grained porous medium. This differs from a free gas, where thermal conductivity is pressure independent due to the fact that at low pressure there are fewer molecules to transfer heat, but the mean free path of each of the particles increases. In a porous medium, thermal conductivity drops with decreasing pressure as the mean free path cannot increase beyond the diameter of a pore.

[46] In addition to gas collisions, deposition of a water vapor molecule on a grain surface can also transfer heat. In our experiment, the fluxes associated with advected heat by water molecules and latent heat of their condensation are small compared to the heat flux from needle pulses and hence are neglected. The fastest observed deposition rate is 2×10^{-3} kg m^{-3} s^{-1}, about 2–4 times the average rate [*Hudson et al.*, 2009], and a latent heat of deposition of 2,585 kJ kg^{-1} (at 237 K) is assumed. This fastest observed deposition is equivalent to a pulse of 0.96 W m^{-1}, less than 9% of the heat delivered by a typical needle measurement, excluding any heat lost upon sublimation which would reduce this value. The time-integrated latent heat transfer was found to cause the overall thermal gradient to be slightly nonlinear for the highest deposition rates [*Hudson et al.*, 2009], but we do not believe this affected individual measurements.

[47] At high temperatures radiative conduction, λ_r, can dominate over λ_{bs}. The radiative component of conduction varies as T^3 [*Schotte*, 1960; *Watson*, 1964; *Cuzzi*, 1972]. This T^3 relation follows from a balance of the radiative heat flow (radiating proportional to T^4) between two grain surfaces. For 1 mm sized particles, radiation does not become a considerable factor in heat transport until a temperature of about 400°C (1500°C for 0.1 mm) [*Schotte*, 1960] so it is negligible for icy regolith.

4.2. Addition of Ice to a Porous Media

[48] Assuming slow deposition, the effect of ice on heat transport is primarily due to the geometry of the ice connections within pores. Ice introduced into a dry porous medium by vapor transport has been theorized to first form at grain contacts [*Mellon et al.*, 1997], the concave meeting point of any two grains. The inward curvature at these contacts causes a lower saturation vapor density in the gas above the surface, similar to the process of evaporation-condensation sintering [*Hobbs and Mason*, 1964]. Through its influence on the cross section available for conduction, such sintered ice necks may rapidly increase thermal conductivity with relatively little ice cement [*Mellon et al.*, 1997; *Piqueux and Christensen*, 2009b]. If ice instead fills the voids between grains homogeneously, one might expect smaller increase in conductivity with ice content. A lower conductivity trend of this sort is observed in thermal properties

measurements of permafrost on Earth [*Johansen*, 1975; *Farouki*, 1981; *Lachenbruch et al.*, 1982] that have experienced a liquid state (or temperatures near 0°C) in the recent past.

[49] *Mellon et al.* [1997] and later *Piqueux and Christensen* [2009b] applied the sintering theory to ice/cement welded soils on the Martian surface. The curvature of the grain causes a local vapor density gradient with a higher density above the convex surface and a low density above the grain contact. Thus, the shape of the grain itself creates a gradient in chemical potential between the overall grain surface and grain contact points. In this theory, explored in more detail in section 6, this density gradient acts as a force to drive molecules toward the contacts and form necks which, in our case being made of highly conductive ice, will greatly increase the solid conductivity of the material.

[50] Assuming ice deposits at these low free-energy contacts, one can directly relate the diameter of the conductive neck to its volume. *Hobbs and Mason* [1964] solve the neck geometry as: $V_{neck} = \pi^2 x^4/(4r_{grain})$, $A_{neck} = \pi^2 x^3/r_{grain}$, and $r_{neck} = x^2/(2r_{grain})$ where V_{neck} is the neck volume, A_{neck} is the surface area of the neck exposed to gas, and r_{neck} is the radius of curvature of the neck. r_{grain} refers to the grain radius and x to the cross-sectional neck radius. The cross-sectional area of the neck (the conduction pathway) is πx^2. Using this geometry, *Mellon et al.* [1997] recognized that the fractional area of the pore space which ice adds to heat conduction, f_A, can be approximately represented by the square root of the fractional volume of the pore space taken up by ice, such that $f_A = \sqrt{F}$. This model treats the heat conduction across a pore as

$$\lambda_p = (1 - f_A)\lambda_{p0} + f_A\lambda_{ice}. \tag{22}$$

Adding this contribution in parallel, the bulk conductivity behaves as

$$\lambda = \frac{\lambda_s\lambda_p}{(1-\epsilon_0)\lambda_p + \epsilon_0\lambda_s}, \tag{23}$$

where λ_s is the conductivity of the grain material and λ_p is the conduction across the pores. λ_{p0}, the conduction across the pores with zero ice content, is found by inverting this equation and setting λ_p to λ_{p0} (which is essentially λ_g) and setting λ equal to λ_{dry}, the bulk thermal conductivity of the ice-free beads. In this paper, λ_{dry} is taken to be 0.068 ± 0.011 W m^{-1}K^{-1} at 6 mbar, in agreement with our measurements at 298 K. Measurements were also taken at lower temperatures, but a discernable trend in thermal conductivity was not found within error. The thermal conductivity of ice, which varies strongly with temperature, $\lambda_{ice}(T)$, is taken to be (488.19/T + 0.4685) W m^{-1} K^{-1} [*Hobbs*, 1974].

[51] Multiple icy soil conductivity models exist for terrestrial applications. They are typically obtained from empirical fits to data rather than physical models [*Sass et al.*, 1971; *Johansen*, 1975; *Farouki*, 1981; *Lachenbruch et al.*, 1982]. As terrestrial permafrost is invariably undergoing a succession of freeze-thaw cycles, these models may be inapplicable to vapor derived ice. Indeed, warmer periods in which water is liquid will allow surface tension to dominate ice structure. In addition, such empirical models could break down in situations of low pressures and temperatures.

[52] Fitting data from *Kersten* [1949], *Johansen* [1975] adopted a weighted geometric mean model for ice with entirely filled pores (F = 1),

$$\lambda_{(F=1)} = \lambda_s^{1-\epsilon_0}\lambda_{ice}^{\epsilon_0}. \tag{24}$$

Johansen's original model included a third term for liquid water, which was present in the Kersten data, but has been removed here as by *Farouki* [1981]. The thermal conductivity of partially filled, icy regolith can then be written as the linear interpolation,

$$\lambda = (\lambda_{(F=1)} - \lambda_{dry})F + \lambda_{dry}. \tag{25}$$

This model implies that terrestrial permafrost structures are dominated by nucleation sites other than grain contact points.

[53] Another simple model for ice is a volumetric mix of ice and soil properties, as occurs with density dependent properties like volumetric heat capacity. This results in the relation

$$\lambda = \lambda_{dry} + \epsilon_0\lambda_{ice}F, \tag{26}$$

which is called the volumetric mixing model throughout this paper. However, predictions by this model will likely break down at high ice contents for which the conduction will no longer be dominated by grain contact points, but by heat transfer through the bulk solids.

[54] A gas component can be added to any of these models by splitting λ_{dry} into a dry conduction in vacuum component, λ_{bs}, and a gas conduction component, λ_g (but is not done so in this study due to lack of precision). Figure 5 compares these simple models as a function of grain filling fraction (assuming ϵ_0 = 43% and T = 237 K, which was chosen to be midway within our measured temperature extremes) in terms of thermal conductivity and thermal inertia.

[55] Many other empirical models are reviewed by *Farouki* [1981]. Other models include intricacies of grain size, fraction of unfrozen water content, and air inclusion in voids [*De Vries*, 1952; *Mickley*, 1951; *Gavriliev*, 2008], but have more detailed dependencies than appropriate to this study. Many of these models are derived from the same *Kersten* [1949] measurements, which were made on ice/soil/water mixtures, and may not apply to vapor deposited ice.

5. Results

5.1. Dry Soil and Pure Ice Measurements/Calibration

[56] A first order calibration of the thermal properties in Mars-like environment was performed by comparison with results of *Presley and Christensen* [1997b] and is shown in Figure 6. "Upper" needle data is data measured by the needle directly above the heated needle, "lower" is measured by the needle below, and "cooling" is data taken from the cooling of the heated needle itself. The *Presley and Christensen* [1997b] measurements were performed using the same glass spheres (Jaygo Dragonite), but with various grain size distributions. Their closest comparable grain size distribution to the 500–600 μm diameter grains used in our experiment was a 500–520 μm distribution.

[57] Our single and dual needle measurements (using only cooling curve data) were found to be consistently lower than

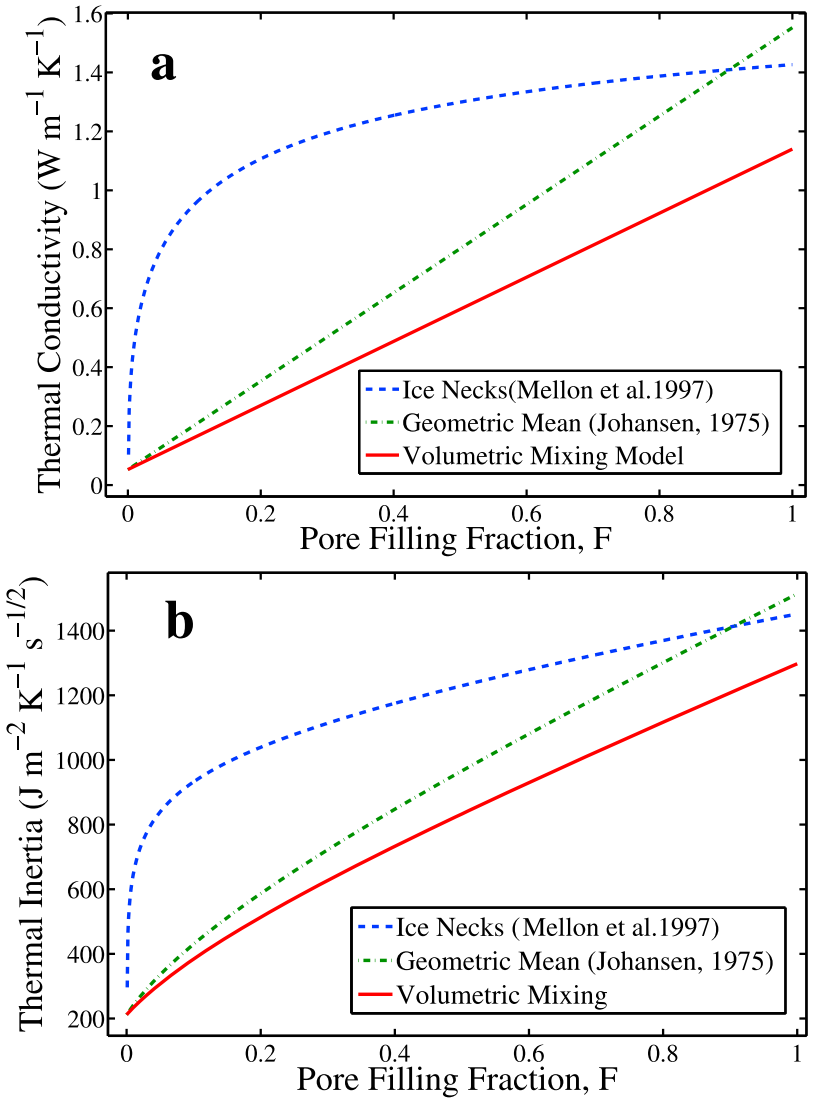

Figure 5. Three possible models of thermal conductivity (a) and thermal inertia (b) of ice-filled porous media with thermal properties of dry 500 micron glass spheres ϵ_0 = 43% porosity and T = 237 K.

the *Presley and Christensen* [1997b] measurements (at pressures above ~4 mbar by a factor of ~0.8). Dual needle measurements (derived from dual needle thermal diffusivity and calorimeter derived heat capacity, see section 5.3) were found to be slightly higher than those of the single needle. Possible sources for this discrepancy from the *Presley and Christensen* [1997b] data are variations in grain packing geometry, density, and grain size distribution between the two experiments. Their experiment used a narrower particle size distribution (500–520 μm diameter) and they reported densities of 1800 kg m^{-3}, as opposed to our 500–600 μm diameters with 1570 kg m^{-3}.

[58] The small discrepancy between the dual and single needle results is likely an effect of contact resistance. A poor contact will result in a change in the total heat loss into the surrounding media (impacting the single needle and the dual needle heat capacity measurements), but not affect the rate heat transfers through the medium (having a negligible effect on the dual needle thermal diffusivity measurement). Therefore, for our relatively short pulses, single needle derived thermal conductivity is expected to generally fall below the more robust dual needle/calorimetric measurements [*Cull*, 1978].

[59] Figure 6 also illustrates the *Presley and Christensen* [1997b] model (black, solid line) for 500 μm spheres with $\lambda = (CP^{0.6})d^{(-0.11 \log p/K)}$ where C and K are constants 1.5 × 10^{-3} and 8.1 × 10^4 torr respectively for pressure P in torr, and grain diameter d in μm. This model, which was fit to many grain sizes (~10–900 μm), matches our data within the same margins as the 500–520 μm *Presley and Christensen* [1997b] data, again showing that variations with grain size and packing can be substantial.

[60] The pressure dependence seen in Figure 6 is interpreted to be due to gas conductivity. Therefore, the conductivity of a dry medium is dominated by the pore-filling gas [*Presley and Christensen*, 1997a; *Slavin et al.* 2002; *Piqueux and Christensen*, 2009a]. As ice fills pore spaces, thermal conductivity (and diffusivity) of the gas component of the dry media is expected decrease, but is not explicitly accounted for in the models presented in section 4.2.

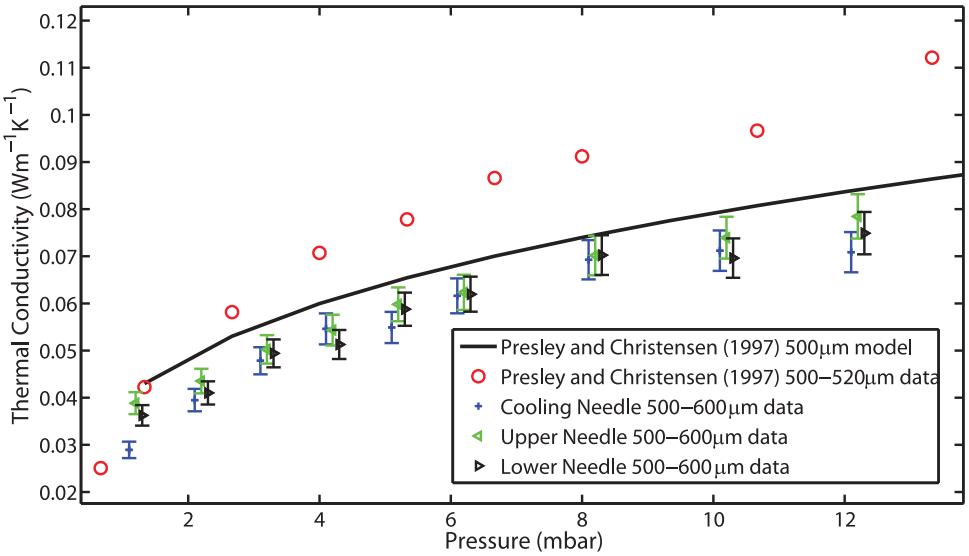

Figure 6. Thermal conductivity of dry regolith simulant (500–600 μm glass spheres) in CO_2 at 1 to 12 mbar as compared to *Presley and Christensen* [1997b] models and data. The lower values of our data imply a slightly differing grain distribution and packing. Pressures are offset by 0.1 (for "Cooling," or single needle cooling curve), 0.2 (for "Upper" dual needle), and 0.3 (for "Lower" dual needle) mbar for clarity.

[61] Pure ice represents another point of calibration. An ice sample was made by freezing water from the bottom of the sample upward, maintaining an ice free surface with the heating lamp to allow trapped gas to escape. Maintaining the ice at a temperature of ~259 K, both dual and single needle measurements of thermal conductivity are found to approximately match the theoretical value of 2.34 W m^{-1}K^{-1} [*Hobbs*, 1974] with 2.41 ± 0.41 W m^{-1}K^{-1} and 2.35 ± 0.42 W m^{-1}K^{-1} respectively. Volumetric heat capacity of ice also agree (with theoretical value 1.865×10^6 J kg^{-1}K^{-1} [*Hobbs*, 1974]) at $1.59 \times 10^6 \pm 0.32 \times 10^6$ J kg^{-1}K^{-1}. Thermal diffusivity (with theoretical value 1.26×10^{-6} m^2 s^{-1}) is measured as $1.29 \times 10^{-6} \pm 0.22 \times 10^{-6}$ m^2 s^{-1}. These agreements imply contact resistance is not a factor when good thermal contact between the needles and the medium (in this case the ice) exists. Once enough ice is emplaced, the vapor-filled samples are conjectured to be in good thermal contact with the needles.

[62] Experiments were run for various durations (see Table 1), then sampled to determine volumetric ice content. Figures 7a and 7b illustrate basic quantities derived from these measurements. The experiment plotted in Figure 7

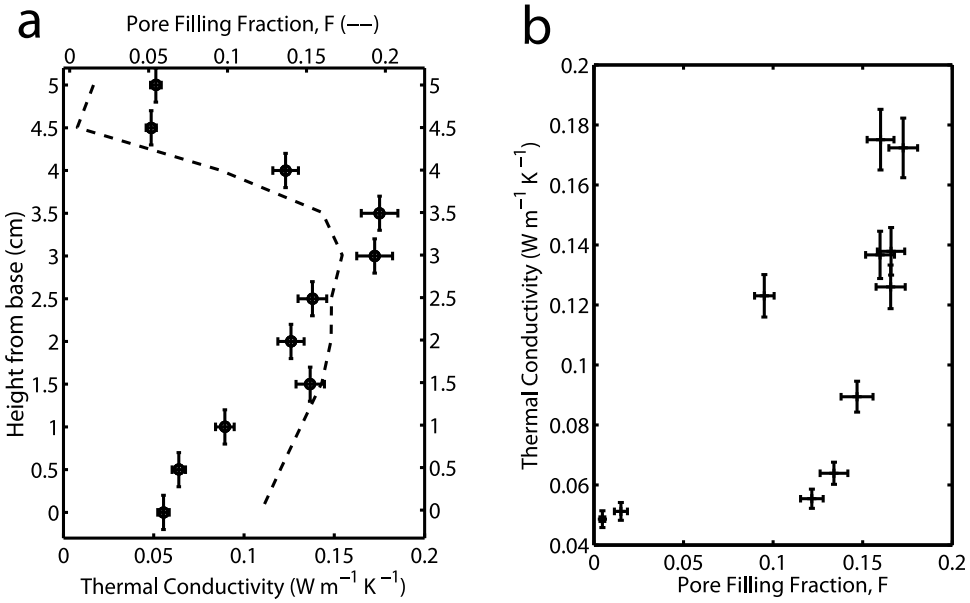

Figure 7. Data from a 24 h experiment. (a) Void filling fraction (dashed curve, top axis) and thermal conductivity (single needle cooling data, bottom axis) as a function of depth within the sample cup. (b) Void filling fraction versus thermal conductivity.

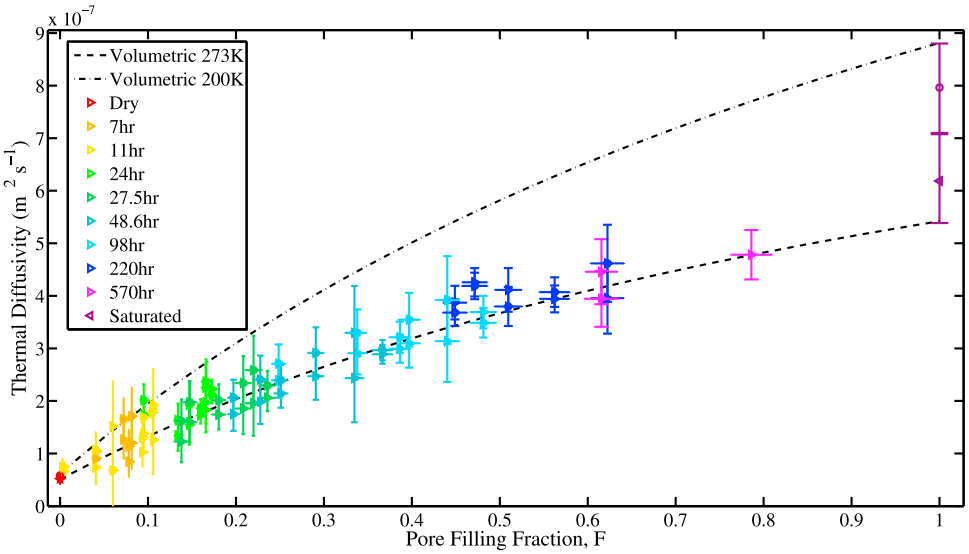

Figure 8. Thermal diffusivity in the vertical direction, κ_z, as a function of ice content as measured by the dual-needle method. Error bars are discussed in Appendix A. The dashed lines correspond to a linear volumetric mixing model in thermal conductivity and heat capacity discussed in sections 2.2 and 5.4.

(24 h in length) shows single needle derived conductivity. Individual measurements show an upward trend in conductivity for higher ice content data (Figure 7a). Figure 7b illustrates how thermal conductivity and volumetric filling fraction vary with depth. There is a general increase in thermal conductivity with ice content, but increasing far more rapidly in more ice-rich layers.

5.2. Dual Needle Data: Thermal Diffusivity and Nominal Volumetric Heat Capacity

[63] Dual needle measurements can be used to derive thermal diffusivity in the vertical direction, κ_z, and nominal volumetric heat capacity, $\rho c\sqrt{\kappa_x/\kappa_z}$ (which assumes no contact resistance). κ_z, is nearly unaffected by anisotropy and contact resistance, but like the single needle data $\rho c \times \sqrt{\kappa_x/\kappa_z}$ is intimately intertwined with anisotropic ice structure. Figure 8 shows all data for dual needle thermal diffusivity, κ_z, evaluated with equations (20) and (21) as explained in section 3.2 (with errors described in Appendix A). Unlike the single needle data (see section 5.4), overlapping data at the same ice content from experiments of different duration, and from different depths in the sample, provide consistent measurements of κ_z. Values of thermal diffusivity derived from the same heat pulses but measured in different locations (the "upper" needle directly above the heated needle, and the "lower" directly below) also exhibit values consistent with the overall trend.

[64] A roughly linear trend emerges in κ_z with ice content. Most of this trend falls within the bounds of a simple volumetric mixing model of thermal properties. The dashed lines plotted in Figure 8 result from linear, volumetric mixing trends in conductivity and heat capacity described in equations (3), (27), and (28). The 100% filling fraction ($F = 1$) data points are from liquid water saturated soil frozen under 6 mbar total pressure (see section 5.4).

[65] Figure 9 shows the remaining fit quantity $\rho c\sqrt{\kappa_x/\kappa_z}$, or nominal volumetric heat capacity, which, given an isothermal, isotropic medium will equal ρc. It also assumes no contact resistance, so that q' is equal the nominal value determined by measuring input power to the probe. However, ρc directly scales with volumetric ice content and a theoretical value is easily calculated from component heat capacities. The black lines in Figure 9 show the theoretical value or ρc at 200 K and 273 K, assuming:

$$\rho c = F\epsilon_o c_{ice}(T)\rho_{ice} + c_{dry}(T)\rho_{\text{bulk}} \tag{27}$$

for porosity ϵ_o (about 43% in our loosely packed beds), constant ice density, ρ_{ice}, of 918 kg m^{-3}, and bulk density of the porous media, ρ_{bulk}, of 1570 kg m^{-3} [*Hudson et al.*, 2009], and

$$c_{ice}(T) \approx (7.49T + 90)\ \text{J kg}^{-1}\text{K}^{-1} \tag{28}$$

[*Lide*, 2003]. Our calorimeter measurements were only performed on the dry soil samples and extrapolated to higher ice contents in this manner. The departure of the data from this model is most readily interpreted as an anisotropic thermal diffusivity ($\kappa_x < \kappa_z$) in the ice-rich media surrounding the needles. Contact resistance between the needles or variations in ice structure with temperature or depth cannot be ruled out.

[66] Despite the uncertainty due to these unknowns, the data can be used to provide an estimate of the relationship between κ_x and κ_z. Figure 9 hints that this relationship is approximately described by $\kappa_x = 0.25\ \kappa_z$ for ice contents greater than about 20% pore-filling fraction as plotted by the gray lines. The ratio κ_x/κ_z may be a consequence of the anisotropy in ice deposition caused by our 900–1100 K m^{-1} temperature gradient and may not be expected to be so large in natural environments. The 20% filling fraction value was selected to approximately match the data, but implies that a change in ice structure occurs when ice fully covers or circumvents the glass beads. Smaller particles might be circumvented faster, causing the 20% threshold to scale with grain size.

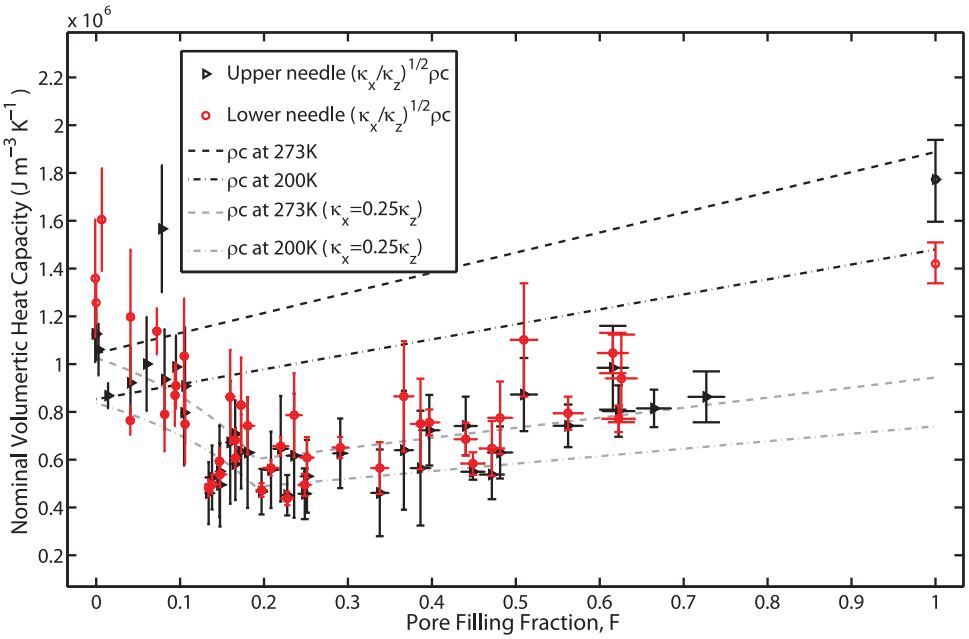

Figure 9. Measured values of nominal volumetric heat capacity, $\rho c\sqrt{\kappa_x/\kappa_z}$ (which assumes all heat from the needles, q', is dissipated into the medium, i.e., no contact resistance), from dual needle data compared to theoretical values of ρc at 273 and 200 K, which match the calorimeter derived values at F = 0. If the medium were isotropic the data should fall between black lines. The gray lines illustrate an anisotropic model where κ_z linearly approaches ~4 times κ_x until 20% filling, then remains fixed at this ratio.

[67] The raw, dual needle measured thermal conductivity will inherently include the same effects due to anisotropy as specific heat capacity and we do not include it here. Thermal conductivity is instead treated in section 5.4 as a combination of the measured thermal diffusivity and the heat capacity expected from a volumetric mixture as measured by the calorimeter. As specific heat capacity is a volumetric property, this assumption acts as a correction for anisotropy.

5.3. Ice Saturated Data

[68] Before proceeding we must briefly address that the ice saturated, or $F = 1$, measurements were not achieved by vapor condensation in our diffusion experiments. Saturated soil may be obtainable by vapor diffusion, but only on extremely long time scales [*Hudson et al.*, 2009]. To obtain a data point for soils with $F = 1$, we prepared a sample of water saturated beads, degassed it under a 6 mbar CO_2 atmosphere, then froze the sample from the bottom up by heating the surface. The lamp was powered at ~35 W to prevent surface ice from forming and trapping gas within the media. Surface water intermittently boiled during pumping to pressures below the saturation vapor pressure, even as ice froze below.

[69] As seen in Figure 8, the $F = 1$ data falls slightly above the trend in thermal diffusivity followed by the vapor deposition experiments. Figure 9 hints that $F = 1$ are not affected by anisotropic ice structures, as the data fall nearly on the expected isotropic trend. This implies that there may be a departure from the simple volumetric mixing model at high ice content. The increase at high ice content may be the result of decreased contact resistance between grains. Alternatively, there may be a change in contact resistance with the needles when liquid water can wet both grain and needle surfaces in a way that does not occur in vapor deposition. In addition, voids trapped within vapor deposited ice may also decrease the effective conductivity of the pore filling ice.

5.4. Thermal Conductivity

[70] Theoretical icy soil thermal properties models are typically expressed in terms of thermal conductivity. However, anisotropic ice structure and contact resistance limit our ability to measure this quantity with needle data alone, as is readily apparent in the single needle thermal conductivity measurements. Figure 10 shows all collected single needle data for the 500–600 μm glass spheres. Similarly to Figure 7a, Figure 10 shows that the highest ice content soils near the ice table in any given sample systematically showed dramatic upturn in thermal conductivity. This effect cannot simply be a function of ice content, as longer duration runs at the same ice content but deeper below the ice table do not reproduce the same conductivity trend. The solid black line illustrates a roughly linear trend of approximately half the slope of the volumetric mixing model represents lower ice content data, away from the ice table, consistent with κ_x = 0.25 κ_z. The rise in thermal conductivity near the ice table may result from a change in the anisotropic structure of the ice or a change of contact resistance with deposition temperature.

[71] This same rise and roughly one-half slope trend is seen in the raw dual needle conductivity, plotted as black circles (derived from measured dual needle thermal diffusivity and nominal volumetric heat capacity). As dual needle measurements are expected to be less sensitive to contact resistance [*Cull*, 1978], this implies that the decreased values in single needle thermal conductivity are mainly a result of

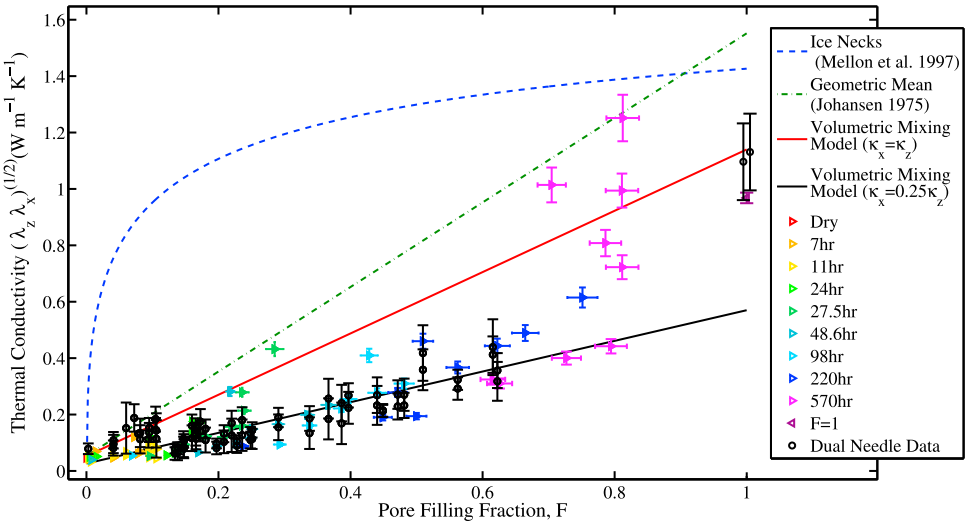

Figure 10. Single needle thermal conductivity as derived from cooling of heated needle assuming an isotropic medium and not including any modeled contact resistance. Each color represents a separate experiment (as listed in Table 1). Black circles correspond to thermal conductivity derived from the dual needle data presented in Figures 8 and 9. Models assume 237 K. Low ice content, colder data follows a linear trend with roughly half the slope of the volumetric mixing model (marked as a black line), which corresponds to $\kappa_x = 0.25\ \kappa_z$, while high ice-content, warmer data is much higher, suggesting a change in pore filling structure with depth.

anisotropic ice structure. The near overlap of these two data sets supports, but does not guarantee, that we are measuring anisotropic thermal structure and not contact resistance with the single needle measurement.

[72] However, the ambiguity introduced by anisotropic thermal structure and contact resistance can be circumvented. Since volumetric ice content is measured separately, one can use volumetric heat capacity as measured from the calorimeter, ρc, to calculate the quantity $\lambda_z = \kappa_z \rho c$ (thermal conductivity in the vertical direction). As discussed in section 5.2, the volumetric heat capacity can be reliably calculated from volumetric mixing (equation (27)) and the vertical diffusivity, κ_z, is essentially unaffected by anisotropy. Figure 11 shows the quantity λ_z (assuming $T = 237$ K for c), which is the most accurate interpretation of the thermal conductivity of the medium in the vertical direction.

[73] The data exhibit a highly linear trend in thermal conductivity as a function of volumetric pore-filling fraction, with a possible rise near 100% pore-filling. The best linear fit to our measured thermal conductivity (not including $F = 1$ data) is $\lambda_z = [(0.876 \pm 0.058)F + 0.0752]$ Wm^{-1}K^{-1}. The intercept roughly matches the dry regolith conductivity ($\lambda_{dry} \approx 0.0675$ Wm^{-1}K^{-1} at 6 mbar measured at 298 K), and can be approximated as $(0.876\ F + \lambda_{dry})$ Wm^{-1}K^{-1}. The

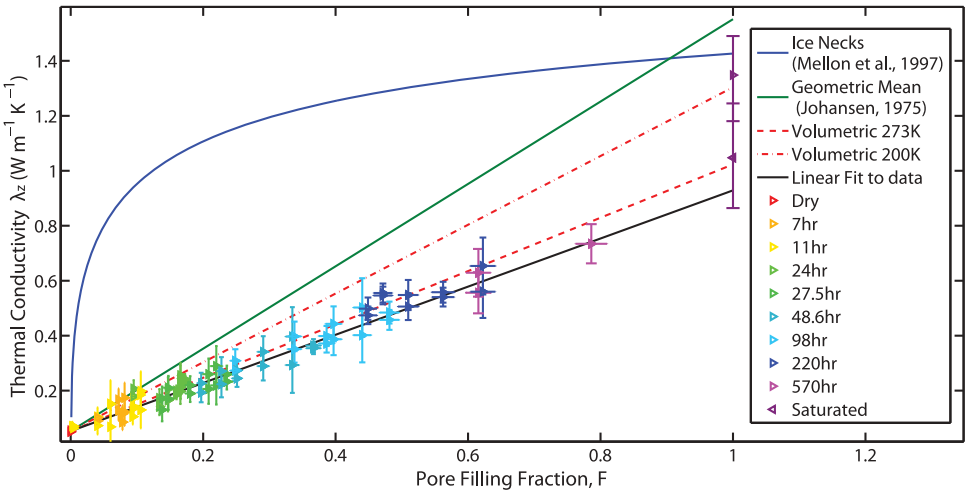

Figure 11. Thermal conductivity in the vertical direction λ_z as a function of ice content as derived from dual-needle measured thermal diffusivity and calorimetrically derived heat capacity. The solid black line represents the best linear fit, $\lambda_z = [(0.876 \pm 0.058)F + 0.0752]$ W m^{-1}K^{-1}, which falls slightly below the volumetric mixing model. The fit y-intercept is within error of the estimate for dry, glass beads of this size.

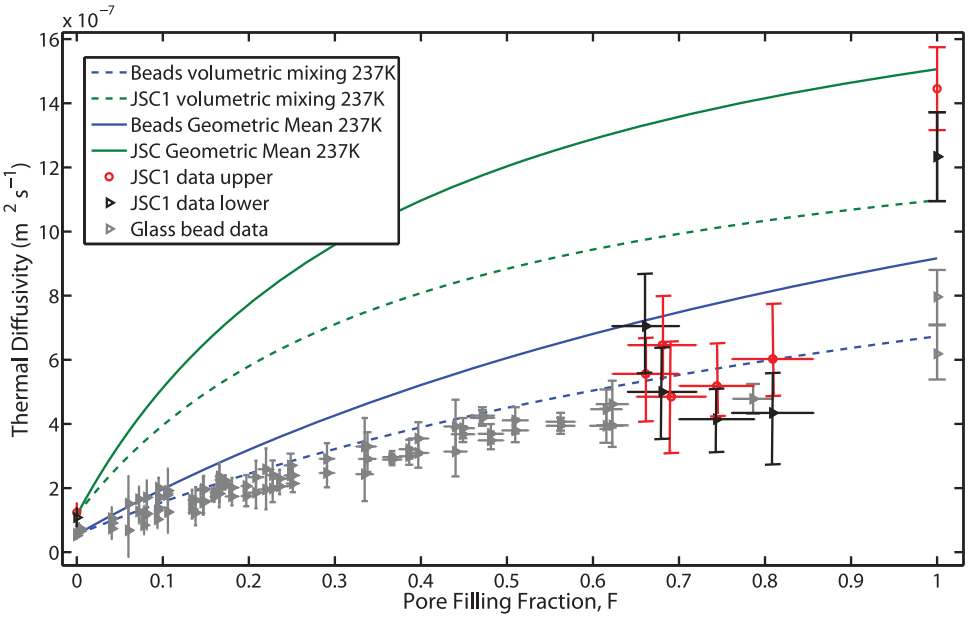

Figure 12. Thermal diffusivity data and models for glass beads and JSC Mars-1. Models assume either the geometric mean model [*Johansen*, 1975] or the proposed volumetric mixing model. Both the glass bead and JSC Mars-1 data fall within the volumetric mixing model for the vapor deposition experiments, but agree more closely with the geometric mean model for the F = 1 experiments. JSC Mars-1 model lines assume 65% porosity, and bead models assume 43% porosity. All models assume 237 K. Variations in temperature and porosity could cause up to 13% error in the JSC model values. The glass bead data from Figure 8 are in gray.

measured values fall at roughly 61% the slope of the value a linear *Johansen* [1975] model and 80% that of the volumetric mixing model is as described in section 4 (at 237 K). A trend line including the $F = 1$ data is best fit by $(1.122\ F + 0.0246)$ $Wm^{-1}K^{-1}$ (which would be ~75% of the Johansen model and ~103% that of the volumetric model).

[74] One clear, and perhaps surprising, result is that our laboratory data shows little resemblance to the expected conductivity of the ice neck model. This is of particular importance to thermal modeling of the Martian environment, where past work typically relied on the assumption that vapor deposition will result in ice necks [*Mellon et al.*, 1997; *Piqueux and Christensen*, 2009b]. The laboratory data implies that our system is not forming sintered ice necks between neighboring grains. Why this occurred, and whether this is also expected to occur on Mars is discussed in further detail in sections 6 and 7.

5.5. JSC Mars-1 Measurements

[75] Of the models presented, the volumetric mixing model best represents our experimental data. However, data taken in saturated glass spheres, with an average conductivity of 1.31 W $m^{-1}K^{-1}$, fall close to the Johansen geometric mean model (1.54 W $m^{-1}K^{-1}$), implying that the soil-independent, volumetric mixing model breaks down at high ice content (it predicts 1.10 W $m^{-1}K^{-1}$). This suggests the best fit model might be one resembling the volumetric mixing model at low to moderate ice contents, but increasing toward the geometric model at greater than ~80% pore filling when grains become fully interconnected.

[76] A second hypothesis could be that the geometric mean model [*Johansen*, 1975] best explains the data, but a lower than expected thermal diffusivity/conductivity occurs due to unusual grain connecting structures. In this second model, when ice contents are between 80 and 100% this pore structure becomes so full that soil grains can be considered fully cemented and contribute to the thermal conductivity as Johansen predicted. This model would predict far higher thermal diffusivity (and conductivity) at mid-range ice contents than the volumetric mixing model hypothesis.

[77] One can differentiate between these two models (volumetric mixing with an upward trend at high ice content and a void-rich geometric mean model) by measuring a material with a different thermal conductivity, λ_s, than the glass beads. With a larger λ_s, the first model would imply a larger jump in thermal conductivity between the vapor deposited experiments and $F = 1$ data. This experiment also gives us an opportunity to explore the effect of natural particles on ice deposition. If our glass beads are hydrophobic, ice deposited by vapor deposition on natural, irregular grains might not show the same volumetric mixing model trend.

[78] Both for its increased solid conductivity and its use as a standard proxy for typical Martian basalt we preformed further tests with JSC Mars-1 regolith simulant [*Allen et al.*, 1998; *Seiferlin et al.*, 2008]. Figure 12 compares our sorted JSC Mars-1 to models and glass bead measurements at a few selected levels of pore filling. As there is a large uncertainty in porosity, we plot thermal diffusivity to minimize errors in the data. We assume 2.0 W m^{-1} K^{-1} for λ_s of JSC Mars-1.

[79] It can again be seen that for a saturated sample, thermal diffusivity values are far higher than those obtained in pore filling experiments. We interpret F = 1 values as falling more in line with the Johansen geometric mean model. However, values obtained in filling experiments

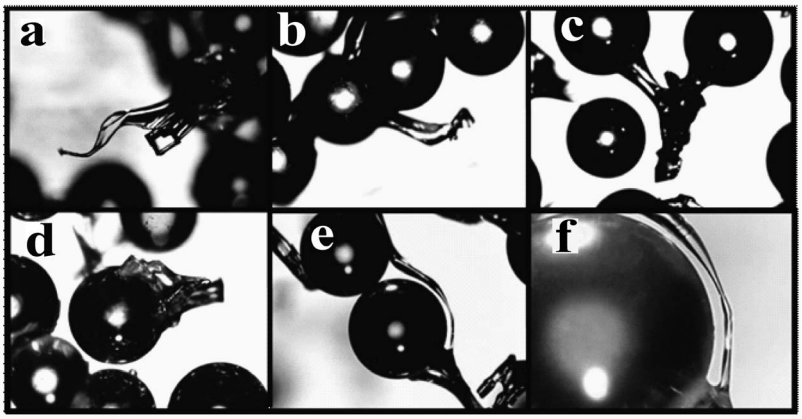

Figure 13. Microscopic images of the 11-h long experimental run at (a–e) 50× magnification and (f) 100× magnification (a close-up of Figure 13e). The spheres, ~500 μm in diameter, act as a natural scale bar. Extended "ice tendril" structures dominate over neck-like structures.

(269 h results are plotted here) show that all vapor-filled samples fall closer to, and even lower than, those expected by the volumetric mixing model. We suggest that the volumetric model best explains the vapor deposition data as proposed by the first hypothesis above. In this model, the non-ice soil matrix has little to no effect on the bulk thermal conductivity at lower ice contents (below the maximum filling fractions achieved in the filling experiments), but a large rise in thermal conductivity occurs between 80% and 100% volumetric pore-filling. The difference between the vapor filled and $F = 1$ data may be a result of bubbles and voids trapped within the ice that may both inhibit heat transfer and preserve anisotropic heat flow as discussed in section 6.

6. Microstructure of Vapor Deposited Ice

6.1. Microstructure: Low Ice Content

[80] The linear trend of thermal conductivity with ice content demands a closer look at the microstructure of the ice formations. To examine the pore-filling structure of the ice, we inspected samples under a microscope both at low and high ice contents. Samples with small ice content were examined in the Caltech Mars and Ice Simulations Lab immediately after the completion of each experiment to avoid a delay that could lead to redistribution of ice under earth atmospheric conditions. High ice content images were taken at the Jet Propulsion Laboratory's Ice Physics Laboratory, within 2 days of the experiment completion, but kept at dry ice temperatures to again avoid redistribution of ice.

[81] The low ice content images, shown in Figure 13 from samples run for 11 h at 6 mbar, show a variety of features best described as extended ice necks or ice tendrils (Figures 13a–13f). Rather than form a neck to an abutting grain, the ice instead grows filaments stretching outward, connecting distant grains. Figures 13a–13c illustrates different stages in the growth toward a neighboring grain. Figure 13a illustrates the occasional dominance of large crystals. Figure 13d illustrates how multiple nucleation sites might join to form parallel fingers which adjoin above the surface. Figures 13e and 13f (a close-up of Figure 13e) illustrate a tendril growing around a grain, rather than contacting its surface. Neck-like features have been reported in previous experiments [*Hudson et al.*, 2009], but while they exist, we find these neighboring grain connections are rare and do not dominate the ice distribution.

[82] The observations suggest nucleation at sites at grain contacts are not favored due to their curvature as models have suggested [*Hobbs and Mason*, 1964; *Mellon et al.*, 1997]. As can be seen in the microscope images (example: Figure 13f) the glass beads are relatively smooth. Since they were also washed in de-ionized water prior to each experiment, there should also be few smaller dust particles on the grain surfaces to act as nucleation points. Therefore, compared to rough, textured grains found on the Martian surface, these beads are expected to favor nucleation at contact points, because they are the sole point of extreme negative curvature.

[83] However, if there is a temperature difference between neighboring grains, a gradient in saturation vapor density due to temperature can also exist. The change in vapor pressure due to curvature (for spherical grains) can be estimated using the Kelvin equation [*Hobbs and Mason*, 1964]:

$$p_{sv,curved} = p_{sv} \exp\left(-\frac{2\gamma V_m}{RTr}\right) \tag{29}$$

where p_{sv} is the saturation vapor pressure over a flat surface, γ is the surface tension of solid ice, R is the universal gas constant, T is the absolute temperature of the grains, and r is the radius of curvature of the surface (for convex surfaces $r > 0$, for concave, $r < 0$). The surface free energy of the crystal interface is 0.033 N m^{-1} [*Hobbs and Ketcham*, 1969]. Adding the surface energy of the liquid-vapor interface of 0.076 N m^{-1} yields γ = 0.109 N m^{-1} for the solid vapor interface [*Gundlach et al.*, 2011]. The molar volume is written as V_m (~18×10^{-6} m^3 mol^{-1} for water). For $r = -10^{-6}$ m and T = 250 K the relative vapor pressure difference across a surface can be calculated,

$$\frac{p_{sv,curved} - p_{sv}}{p_{sv}} = \frac{\Delta p_c}{p_{sv}} \approx -\frac{2\gamma V_m}{RTr} = 2 \times 10^{-6} \tag{30}$$

Meanwhile, the local difference in partial pressure caused by the temperature difference across a grain (diameter d) can be approximated as

$$\Delta p_T = \frac{\partial p_{sv}}{\partial T} g d, \tag{31}$$

where p_{sv} is the saturation vapor pressure

$$p_{sv}(T) = p_t \exp\left[-\frac{Q_{LH}}{R}\left(\frac{1}{T} - \frac{1}{T_t}\right)\right], \tag{32}$$

with p_t (611.7 Pa) and T_t (273.16 K) are the triple point pressure and temperature of H_2O, and Q_{LH} is the latent heat of sublimation ($Q_{LH}/R \approx 6130$ K). In our experimental setup, with a nominal temperature gradient g = 900 K m^{-1}, assuming the average T of 237 K,

$$\frac{\Delta p_T}{p_{sv}} = \frac{Q_{LH}}{RT^2} g d \approx 0.049. \tag{33}$$

Thus, for our assumed neck radius and temperature gradient the temperature effect exceeds the curvature effect by more than four orders of magnitude (comparing equations (30) and (33)).

[84] The radius of curvature at the contact can be better approximated by examining the grain roughness. Rough grains do not simply touch at a point [*Bahrami et al.*, 2006] and the separation distance at the contact point of neighboring grains can be estimated to scale as twice the surface roughness [*Slavin et al.*, 2002]. Using a MicroXAM optical profiler (ADE Phase Shift Co.) at the UCLA Ion Probe Facility, the average surface of a fresh glass bead was found to have surface imperfections on the order of 2 to 3 μm. That leads to an estimated contact point separation, and therefore radius of curvature of the grain contact of $\sim$0.5 μm.

[85] The radius of curvature will increase with ice content if ice were to form at the contact point. Therefore, ice forming at a grain contact will decrease the curvature driving forces and inhibit further growth at the contact. For random packing an average of 6 grain contacts occur around each void [*Slavin et al.*, 2002], half of which contribute to ice volume within a void, which results in 3 entire neck volumes per unit cell. Assuming a void volume of $V_{void} \approx (4/3\pi\epsilon_o\, r_{grain}^3)/(1 - \epsilon_o)$ [*Slavin et al.*, 2002] and $V_{neck} = \pi^2 x^4/(4 r_{grain})$ as the volume of a single neck with neck radius of curvature $r_{neck} = x^2/(2 r_{grain})$ [*Hobbs and Mason*, 1964], results in the relation

$$r_{neck} \approx \frac{2 r_{grain}}{3} \sqrt{\frac{F \epsilon_o}{\pi(1 - \epsilon_o)}}, \tag{34}$$

which for 500 μm grains and 43% porosity, ϵ_o, even a small F = 0.015 already results in r_{neck} = 10 μm, decreasing the driving force discussed in equation (30) by an order of magnitude.

[86] If instead the temperature gradient is the driving force behind the observed structures, then when $\Delta p_c > \Delta p_T$, as defined in equations (30) and (33), ice necks should be the dominant formation of inter-granular ice. In our experiment, which uses 500 μm spheres with an assumed 0.5 μm radius of cuvature due to grain roughness, temperatures between $\sim$200 and 268 K fall above the transition for gradients higher than about 10^{-2} K m^{-1}. Though local, grain-to-grain gradients have not been measured in our set-up, taking the large scale gradients to be representative of those at the grain scale results in 900 K m^{-1}, five orders of magnitude higher. Therefore, sintered ice necks are not expected to form in our experiment.

[87] The vapor density gradient is dependent both on the local temperature gradient and the absolute temperature. Therefore, for a given gradient at various absolute temperatures, one might expect a transition between curvature dominated (neck-like) and temperature dominated (tendril-like) inter-grain ice formation. Despite having average temperatures gradients much lower than this experimental setup, it is unlikely that surface conditions on Mars, the Moon or other potentially icy bodies cross this boundary. Even the geothermal gradient of the Moon, which would serve as a lower limit for the time averaged gradient, was measured to be 0.79 K m^{-1} or higher [*Langseth et al.*, 1976]. Furthermore, at lower temperature gradients, water molecules will not move efficiently by vapor diffusion. Lower absolute temperatures may cause amorphous, rather than crystalline, ice to dominate [*Schmitt et al.*, 1989].

[88] In light of these considerations, the ice filling structures observed in our experiment can be explained by local temperature conditions. Even the near-perfect grains in this experiment have small surface defects. Water vapor entering a void would be most stable at a small defect on the coldest available grain, where there is both a thermal and Gibbs free-energy advantage due to a possible surface defect with inward curvature. Conversely, the grain contact would present a point of inward curvature with one cool and one warm face. In addition, the high heat flux through the grain contact will cause the contact point in the cold grain to be substantially warmer than the rest of the grain [*Piqueux and Christensen*, 2009a], potentially driving molecules away from, rather than toward, this point. The contact is the coolest point on the warm grain, but is warmer than any point on the cold grain. This would inhibit ice growth at the grain contact, favoring initial ice growth at any other imperfection on the cold bead's surface.

[89] Once ice begins to grow at a cold defect it may be a preferential site for further ice growth, as it maximizes the surface area exposed to the saturated gas. In a saturated environment (as we have below the ice table) this point will continue to gain ice, growing outward from the surface. If there is a nearby, but not directly connected, grain across the pore that is also cold, there will be a lower vapor density near the surface of this grain (attracting water vapor from areas of higher density), aiding in directing the growth of the ice tendril in that direction (as in Figures 13e and 13f). This growth scenario would explain the connection between relatively distant neighbors seen in the microscope images. Figures 13e and 13f illustrate a tendril growing around a grain which, in this scenario, would have been slightly warmer and unfavorable for surface ice growth.

[90] It is also possible that the grain surface is hydrophobic relative to JSC Mars-1 and other natural materials, repelling water molecules that landed there. However, as the hydrophobic and hydrophilic nature of a grain will only affect surface tension, it can be expected that any such surface effect will be on the same order as that from grain curvature (i.e., equation (30)), and therefore be relatively

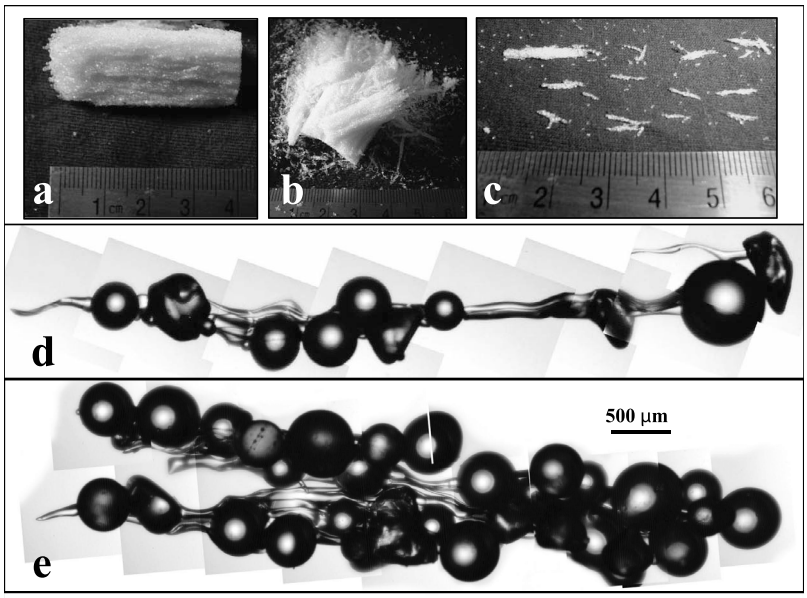

Figure 14. Photographic and microscopic evidence for preferential ice tendril growth in the *z* direction. These samples taken from a 24 hour long experiment, reveal anisotropic ice growth and are consistent with the anisotropic thermal diffusivity observed with the dual needle measurements (as seen in Figures 9–11). (a–c) The large-scale fabric of the ice tendrils. (d and e) The ice linkages that form between individual grains to create tendrils.

unimportant in determining ice formation. Regardless of the cause, molecules being repelled from a grain (i.e., Figure 13f) and neighboring grain surfaces may form a lane of high vapor concentration, along which tendrils preferentially grow. The feature in Figure 13f could be explained by two independent tendrils growing along such an avenue and uniting mid-way.

6.2. Microstructure: Medium Ice Content and Anisotropic Ice Growth

[91] The small scale structures, which appear to be controlled by local thermal gradients, will adjoin to form larger ice formations. The net thermal gradient orients individual tendrils which can join to create long filamentous structures. At low ice content (<∼20% pore filling fraction in our experiment) ice grows primarily along the thermal gradient. At higher ice contents, ice growth proceeds, but the ratio of κ_x to κ_z remains relatively constant (Figure 9).

[92] Figure 14 illustrates a sample from the upper 4 cm of a 24 h long experiment (∼15–20% pore filling fraction). Figure 14a shows a clear fabric of ice connected glass beads which forms a lineation in the vertical (*z*) direction (the sample surface is to the right in these images). Figures 14b and 14c illustrate the filaments of the ice/grain fabric at various stages of dissection. Figures 14d and 14e are microscopic images of the dissected filaments seen in 14c and show that these filaments are constructed of multiple ice tendrils, like those examined in Figure 13. Figures 14d and 14e are oriented in the same manner as Figure 14a, with the sample surface to the right.

[93] We interpret these structures to be responsible for the anisotropic thermal diffusivity observed in Figures 9 and 10. Ice growth, initially controlled by the forces described by equation (33), will preferentially link a grain to its coldest neighbor. Due to the underlying thermal gradient in our sample, that next coldest grain is likely to be lower in the sample. As can be seen in Figures 14d and 14e, the cold grain is often several grains away, and ice often takes tortuous pathways to reach the cold surface. The net results of this growth are heat pathways in the *z*-direction, as implied by the single needle conductivity and dual needle het capacity measurements. The heat capacity measurements suggest that this anisotropic growth stabilizes at about 20% pore filling fraction. At this point, the rate of anisotropic growth slows, maintaining a ratio of κ_x/κ_z of about 0.25. However, as seen in Figures 9 and 10, this underlying anisotropic structure continues to dominate thermal properties until very high ice contents (at least 80%). Our ice saturated ($F = 1$) experiments show no evidence of anisotropic thermal properties.

6.3. Microstructure: High Ice Content

[94] As ice growth continues, tendrils will further intertwine, but, as hinted in the dual needle measurements, will retain an underlying anisotropic structure. Images at high ice contents can aid in interpreting what remnants of the initial pore filling structure control high ice content thermal properties. The images in Figure 15 have been obtained under transmitted illumination with an Olympus BX51 microscope equipped with a LN_2-cooled Linkam LTS 350 cryostage at the Jet Propulsion Laboratory's Ice Physics Laboratory which was pre-cooled to −30°C to avoid any melting of the samples.

[95] Figure 15 shows evidence of voids and bubbles within ice resulting from an experimental run after 570 h. The samples in these images were found to have roughly 75–80% pore filling fraction, *F*, by a gravimetric measure.

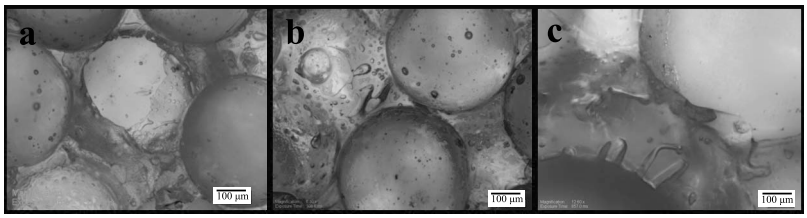

Figure 15. Microscopic images of a sample run for 570 hours. The soils in these images were found to have roughly 75–80% pore filling fraction. (a) Bubbles in ice coating grains. (b) Larger voids between grains. (c) Angularly faceted bubbles believed to be from the growth of intersecting crystals.

Voids within the ice, possible remnants of the initial tendril structure, may contribute to the remaining volume.

[96] Similar structures were observed in low ice content images, Figure 16, showing that some of these voids are trapped gas bubbles, rather than just inter-tendril voids. Such bubbles may record information about the ambient gas present at the time of formation [*Hudson*, 2009].

[97] The voids and bubbles may be partially responsible for the lower than volumetric mixing trend found throughout the data (i.e., Figures 8 and 11). Voids could cause the solid pathways for heat to be disrupted, dropping the overall conductivity expected at a given volume filling fraction. In addition, many voids occur at the grain/ice boundary (i.e., Figure 15c), which would cause an effective contact resistance between the grains and ice. Bubbles and voids are seen between and within tendrils (Figures 15 and 16) and poor contacts were observed at ice-bead interfaces. Adjusting λ_{ice} in equation (26) to account for heat pathways being disrupted by voids and bubbles may bring the volumetric model in closer agreement with the data presented in Figure 11. Additionally growing anisotropic tendrils merge, creating anisotropic voids. These preferentially oriented voids may be responsible for the anisotropy in thermal properties that exists even at high ice contents (i.e., Figures 9 and 10).

[98] It is unknown whether the effect, or even presence, of voids depends upon ambient gas pressure or ice deposition rate. Future experiments could examine these depositional processes over a range of ambient gas pressures, and would benefit from a quantitative measure of trapped gas, rather than our simple photographic survey. Experiments can be performed at lower thermal gradients, but, like natural settings, deposition will be greatly slowed, making such experiments difficult.

[99] Voids and bubbles may also account for the apparent discordance between the vapor-deposition experiments, which follow the volume mixing model (equation (26)), and the ice saturated experiment, which are better fit by the geometric mean model (equation (25)). The saturated samples (section 5.4) trap relatively few bubbles in the pore-filling ice. As water was emplaced into the $F = 1$ sample in a liquid state, this may allow for better thermal coupling between water molecules and the grain surfaces than vapor deposition, increasing the thermal conductivity of the matrix.

7. Applications to the Mars Environment

[100] The observations in this experiment have direct implications for subsurface pore-filling ice present on Mars today. Ice cemented regolith was identified by the Phoenix Mars lander [*Mellon et al.*, 2009]. Though the Phoenix lander did carry a Thermal and Electrical Conductivity Probe (TECP), which our experiment was designed to replicate, real ice rich Martian regolith proved too cemented to emplace the probe needles [*Zent et al.*, 2010].

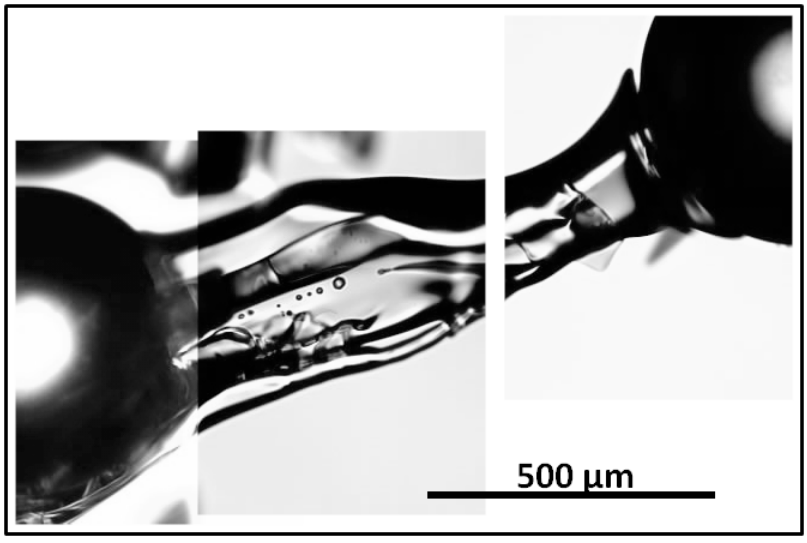

Figure 16. Bubbles formed within an ice tendril during an 11 h experiment.

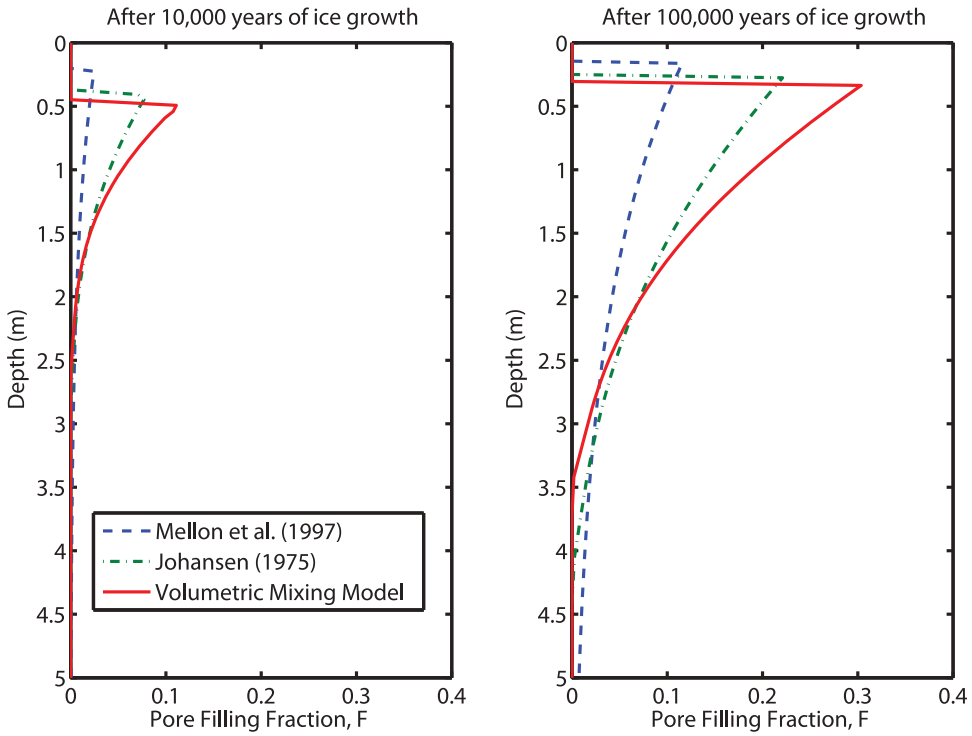

Figure 17. Results of 100,000 year of atmospheric ice deposition into dry regolith with the three parameterizations of thermal conductivity from Figure 5. Models resulting in high thermal conductivity with low ice content will build less ice, but reach more deeply into the subsurface.

[101] Such pore ice may retain the form under which it deposits, or may slowly redistribute throughout pores annealing structures over long time scales, depending on temperatures reached and depth of burial at a given location [*Arthern et al.*, 2000]. Regions that remain permanently cold or uncompacted may be able to retain trapped gasses in these bubbles from the time of ice formation (i.e., Figures 15 and 16).

[102] The difference in thermal conductivity of vapor-deposited ice may also affect the concentrations of subsurface ice as a function of depth. Increased thermal conductivity allows thermal waves to travel deeper while also decreasing their amplitude. Therefore the rate of the build-up of ground ice depends upon which conductivity model is assumed [*Paige*, 1992]. Figure 17 illustrates the effect that each of the three example thermal properties models would have on the long-term deposition model [*Schorghofer*, 2010] assuming the atmospheric humidity and location of the Phoenix landing site (68.22°N latitude) with an assumed albedo of 0.2, soil thermal inertia of $I = 250$ J m^{-2} K^{-1} s$^{-1/2}$, λ_{dry} = 0.0486 W m^{-1} K^{-1}, 28 mW m^{-2} geothermal heat flux, dry soil heat capacity $c = 800$ J kg^{-1} K^{-1}, 1608 kg m^{-3} bulk density with 50% porosity [*Zent et al.*, 2010]. As expected, the ice neck model, in which thermal conductivity increases most rapidly, builds less ice, but the ice extends to greater depths.

[103] There may also be a second transition in ice depositional structure, and therefore thermal properties, near the triple point of water. If liquid water is able to form in thin films on the grain surfaces the dramatic increase in mobility in response to surface tension might cause ice necks and their associated conductivity enhancement to establish, regardless of the initial pore-filling structure. However, if water does not wet soil grains, it may instead adhere to other water molecules, forming ice grains disconnected from the regolith surface (likely following a more linear conductivity model). In combination with other approaches studied to distinguish vapor- from liquid-derived ground ice [e.g., *Lacelle et al.*, 2008], the thermal properties of icy regolith can serve as a marker as to whether the ice present in a given location has ever experienced a liquid state. At low to moderate ice contents, these two structures should result in dramatically different thermal properties. These various thermal conductivity models also have a large effect on ice contents derived from orbital thermal inertia measurements (Figure 5).

[104] For example, a partially filled, icy Martian regolith with only 10% pore filling in the form of isotropic ice necks would have a thermal inertia of about 900 J m^{-2} K^{-1} s$^{-1/2}$ (Figure 5b). A measurement of this thermal inertia, given the volumetric mixing model, would imply approximately 60% volumetric filling. Conversely, a 10% pore filling fraction with tendril features as observed in the lab would result in a modest thermal inertia of only 380 J m^{-2} K^{-1} s$^{-1/2}$. Therefore, if the latter model were a better representation of Martian ground ice, areas mapped as having low thermal inertia and assumed ice poor (or to have deeply buried ice) might be consistent with substantial ice fractions near to the surface [*Paige*, 1992; *Mellon et al.*, 2004; *Putzig and Mellon*, 2007]. Such differences may be hidden in diurnal thermal inertia measurements, which are dominated by very

near surface material that tends to be ice free in deposition models (Figure 17), but may be prominent in more deeply penetrating, seasonal temperature variations.

8. Conclusions

[105] Icy regolith was created in the laboratory by vapor deposition under Martian atmospheric pressure (6 mbar) and sub-freezing temperatures. We have measured the thermal diffusivity with a multineedle probe and the heat capacity with a calorimeter. For this purpose, we have extended the equations for inversion of single and dual needle probe measurements to an anisotropic medium. The thermal conductivity of 500–600 μm sized glass beads and JSC Mars-1 is best fit by a linear volumetric mixing model between ice and dry regolith.

[106] For the glass beads, the quantitative results for thermal conductivity are plotted in Figure 11 and given by

$$\lambda_z(F) = [(0.88 \pm 0.06)F + 7.5 \times 10^{-2}]\ \mathrm{Wm^{-1}K^{-1}} \qquad (35)$$

at $T = 237$ K for pore filling fractions between 0 and 0.75. This is essentially identical to volumetric mixing model, equation (26), except the thermal conductivity of ice is reduced to 80%. Equation (35) can be approximately rewritten as

$$\lambda_z(F,T) = (0.80 \pm 0.05)\epsilon_0\lambda_{ice}(T)F + \lambda_{dry}(T) \qquad (36)$$

within error of our measured λ_{dry}. At different ambient pressures, or under different thermal gradients, the prefactor may differ from 0.80 because thermal conductivity may increase as void and bubble volumes decrease. λ_{dry} also decreases with decreasing pressure (i.e., Figure 6). Thermal diffusivity, κ_z, can be calculated as $\lambda_z/\rho c$ as a function of F and T.

[107] A linear trend is also found in filling experiments with JSC Mars-1 regolith simulant up to approximately 80% volumetric pore filling, as shown in Figure 12. At higher filling fractions than those tested, thermal conductivity rises toward a saturated value and is consistent with the geometric mean of the components given by equations (24) and (25).

[108] Photographic evidence reveals the formation of an inter-grain structure of long ice tendrils (Figure 13). These tendrils differ from ice necks in that ice generally links a grain to a semi-distant neighbor. In the ice neck model, pore-filling ice initially forms links between grains in direct contact with each other. This tendril dominated structure causes thermal conductivity to vary linearly with ice content, as in equation (36).

[109] The absence of ice necks may be understood as an effect of the large thermal gradients that can exist between grains at low atmospheric pressures. Under these conditions, vapor pressure changes caused by the local curvature of a meniscus are typically many orders of magnitude smaller than those caused by temperature differences between grains, as described by equations (29)–(33). Therefore, even under very small local thermal gradients, tendrils should be expected to form along the gradient, rather than isotropic ice neck structures. According to this theory, anisotropic ice structures are obtained even for smaller gradients than are expected in nature.

[110] Our results further indicate that vapor-deposited ice grows anisotropically and preferentially along the direction of the vapor density gradient. Our experimental setup is not designed to accurately measure thermal diffusivity in the horizontal direction, but an approximate value extracted from volumetric averages indicates the ratio of vertical to horizontal thermal diffusivity reaches a factor of roughly four (Figures 9 and 10), and remains so to ~80% pore filling fractions. In addition, microscope images of undisturbed samples whose orientation was maintained shows that the tendrils grow along the thermal gradient and form chains of ice-bonded grains (Figure 14).

[111] Though the temperature gradients in our experiment are larger than the time averaged temperature gradients experienced on Mars and the Moon, the arguments presented here for anisotropic ice growth and void formation should hold under natural conditions. Furthermore, ice will be most mobile in these environments when instantaneous local thermal gradients, which may dominate ice mobility, are high. Depending on the pore-filling geometry, a given thermal inertia can correspond to substantially different ice content (larger than a factor of two at a 10% pore filling fraction).

[112] These experimental results may also have an impact on assumed electrical and diffusive properties of planetary regolith. Thermal and electrical conductivities are often intimately linked and considerations of pore-filling structures may also affect interpretation of ice probed by radar measurements. Vapor diffusion models may also need to account for such structures. The tortuosity of an ice-filled medium may be different if ice forms tendrils rather than necks. Future experiments can attempt to measure these quantities in light of ice formation processes as well as to probe the effects of time varying temperatures and grain size distribution on ice filled thermal properties.

Appendix A: Error Analysis of Fit to Needle Data

[113] Many sources of error are accounted for in the measured thermal properties in this experiment. Errors shown for in derived thermal diffusivities arise from a nonlinear fit and variation in supplied heat (q). Other errors, such as variation in needle spacing and edge effects are neglected, but small in comparison. Data from the lowest needle touching the brass baseplate are not used.

[114] Initially, the measured ΔT values (as illustrated in Figure 4), are fit to equations (8) (for the cooling of the heated needle), (20) or (21) (for the neighboring needles) by a nonlinear least squares regression. The error in the nonlinear fit also contain any uncertainty caused by inadequate time or temperature resolution.

[115] For single needle data (only data from the cooling trend is presented in this paper) best fits for each variable λ, t_c, or d from equation (8) for a 300 s interval are calculated as a fit coefficient, residual, and Jacobian. To find the relative error in single needle thermal conductivity result, the relative error of a 95% confidence interval in the fit to λ is added in quadrature with the relative error in q' (which includes uncertainties in current 0.109 ± 0.006 A, voltage 6.00 ± 0.01 V, and length 0.060 ± 0.001 m). This typically gives a relative error of ~6% a given measurement (vertical error bars in Figures 7, 9, and 10). The effect of contact

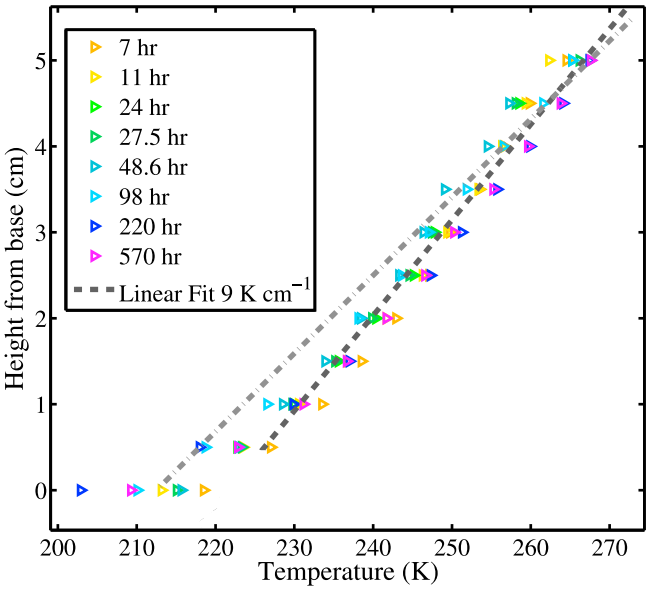

Figure A1. Linear approximations of the thermal gradient throughout the sample as compared to thermocouple data taken during the ice filled measurements listed in Table 1. The 9 K cm^{-1} fit did not include the bottom needle, which was in contact with the brass base plate. The 11 K cm^{-1} gradient represents the average gradient, including the bottom needle.

resistance and anisotropy are not accounted for in single needle measurement error bars.

[116] Dual needle error calculations are treated similarly with nonlinear fits to κ_z and $\rho c\sqrt{\kappa_x/\kappa_z}$ in both equations (20) and (21). As pulses in low conductivity materials take longer to reach neighboring needles, this fitting interval was varied between 200 and 700 s after the initiation of the heat pulse with length t_0. The effect of the gradient is taken into account by subtracting the average temperature at the sensing needle of a 100 s interval prior to the heat pulse, equations (20) and (21).

[117] This method, and those discussed in section 3.2 are only strictly valid if the overall thermal gradient is truly linear. Any nonlinearity in the gradient could introduce an error in equations (10)–(21), which include the assumption $\Delta T(x, z, t) = T(x, z, t) - gz$. Figure A1 shows the measured temperature profiles at the point in time in each experiment that the data in Figures 7–11. Other than the bottom-most needle, not included in our analysis, a roughly linear ~9 K cm^{-1} gradient was found to approximate data within <3 K. Including the bottom needle, the overall average gradient could be considered as large as 11 K cm^{-1}.

[118] Errors in volumetric filling fraction, fraction, $F = \sigma/\sigma_0$ (horizontal error bars in Figures 7–12) were obtained as described by *Hudson et al.* [2009]. Errors in filling fraction are obtained by propagating errors in m_t, m_s, ρ_{bs}, and ρ_s with an assumed measurement error of 2 × 10^{-3}g in mass measurements and 10 kg m^{-3} error in bulk density. For JSC Mars-1, ρ_s was assumed to have a 10% error.

[119] Samples were sliced at approximately 0.5 ± 0.05 cm intervals (roughly between needles) and assigned to the thermal properties measurement of the nearest neighboring needle. The temperature changes across the top and bottom of the sample from 268 to 193 K. Over this range, the conductivity of pure ice changes from 2.22 W m^{-1} K^{-1} to 3.30 W m^{-1} K^{-1} [*Lide*, 2003]. The thermal diffusivity changes between 1.17 × 10^{-6} m^2 s^{-1} and 2.38 × 10^{-6} m^2 s^{-1}. For a dry sample, the temperature dependence is smaller than our measurement errors. The temperature dependence of the glass bead thermal conductivity is assumed 1.5 × 10^{-3} $(T - 273) + 1.1277$ Wm^{-1}K^{-1} (for temperature T in K, fit from Sciglass™ program) and varies between 0.71 and 0.61 W m^{-1} K^{-1} and the sign of the temperature dependence is opposite from that for pure ice. Using equation (26) and a porosity of 43%, we find that λ_z for a completely ice-filled sample should vary by about 10%, due to the temperature dependence of the ice, and by 3% due to the temperature dependence of the soil simulant. The temperature dependence of any contact resistance is unknown. Therefore we add 5% about the value adjusted to 237 K to all our errors, the remaining 3% temperature dependence counteracts this trend and is, in any case, much smaller than other sources of error.

[120] Uncertainties in volumetric heat capacity are propagated through equation (27). The relative error in volumetric heat capacity is determined by summing in an error in filling fraction described above with an additional 2% relative error in porosity in quadrature. Relative errors in the calorimeter measured $c_{dry}(T)$ are negligible (Figure 3). JSC Mars-1 data was determined in the same fashion, but given a 10% uncertainty in porosity.

[121] A good estimate of thermal properties is also possible on the basis of the time and magnitude of temperature rise and a detailed discussion of the errors associated with this method of fitting the data is given by *Kluitenberg et al.* [1993].

Notation

F pore volumetric filling fraction, no unit (or % × 100).
P total atmospheric pressure, Pa.
T temperature, K.
c_{dry} heat capacity of dry beads, J K^{-1} kg^{-1}.
c_{ice} heat capacity of ice, J K^{-1} kg^{-1}.
g temperature gradient, K m^{-1}.
p_{sv} saturation vapor pressure, Pa.
q heat per unit length, J m^{-1}.
q' heat per unit length per unit time, W m^{-1}.
t time, s.
t_o length of pulse, s.
x horizontal distance, m.
z vertical distance, m.
ϵ_o porosity, no unit (or % × 100).
κ thermal diffusivity, m^2 s^{-1} (subscript implies direction).
λ_{dry} thermal conductivity of dry medium (including gas), W m^{-1} K^{-1}.
λ_{ice} thermal conductivity of bulk ice, W m^{-1} K^{-1}.
λ_s thermal conductivity of the solid material, W m^{-1} K^{-1}.
λ_{bs} thermal conductivity of bulk, porous solid (in vacuum),W m^{-1} K^{-1}.

ρ_{bulk} bulk density of the porous medium, kg m^{-3}.
ρ_{ice} density of bulk ice, kg m^{-3}.
ρ_s density of the solid material, kg m^{-3}.

[122] **Acknowledgments.** We thank Julie Castillo, Doug Cobos, Michael Hecht, Gerard Kluitenberg, Kenneth Libbrecht, Michael Mellon, David Paige, Marsha Presley, Al Slavin, and Steven Wood for their useful discussions and Axel Schmidt for aid in measuring grain surface roughness, Karen Wacker for the construction of and insightful discussion in designing our thermal properties probe, and Hermann Engelhardt, Liz Carey, and Kenny Oslund for years of guidance and dedication in the lab. This work was supported by the Mars Fundamental Research Program. Part of this work has been conducted at the Jet Propulsion Laboratory, California Institute of Technology, under contract to NASA. Government sponsorship acknowledged.

References

Allen, C. C., R. V. Morris, D. J. Lindstrom, M. M. Lindstrom, and J. P. Lockwood (1998), JSC Mars-1: Martian regolith simulant, *Lunar Planet. Sci.*, *XXVIII*, Abstract 1259.

Arthern, R. J., D. P. Winebrenner, and E. D. Waddington (2000), Densification of water ice deposits on the residual north polar cap of Mars, *Icarus*, *144*, 367–381, doi:10.1006/icar.1999.6308.

Bahrami, M., M. M. Yovanovich, and J. R. Culham (2006), Effective thermal conductivity of rough spherical packed beds, *Int. J. Heat Mass Transfer*, *49*, 3691–3701, doi:10.1016/j.ijheatmasstransfer.2006.02.021.

Bristow, K. L., R. D. White, and G. J. Kluitenberg (1994), Comparison of single and dual probes for measuring soil thermal properties with transient heating, *Aust. J. Soil Res.*, *32*, 447–464, doi:10.1071/SR9940447.

Campbell, G. S., K. Calissendorff, and J. H. Williams (1991), Probe for measuring soil specific heat using a heat pulse method, *Soil Sci. Soc. Am. J.*, *55*, 291–293, doi:10.2136/sssaj1991.03615995005500010052x.

Carson, J. K., S. J. Lovatt, D. J. Tanner, and A. C. Cleland (2005), Thermal conductivity bounds for isotropic, porous materials, *Int. J. Heat Mass Transfer*, *48*, 2150–2158, doi:10.1016/j.ijheatmasstransfer.2004.12.032.

Christensen, P. R., and H. J. Moore (1992), The Martian surface layer, in *Mars*, edited by H. H. Kieffer et al., pp. 686–729, Univ. of Ariz. Press, Tucson.

Cremers, C. J. (1971), Thermal conductivity cell for small powdered samples, *Rev. Sci. Instrum.*, *42*, 1694–1696, doi:10.1063/1.1684970.

Cremers, C. J., and H. S. Hsia (1974), Thermal conductivity of Apollo 16 lunar fines, *Proc. Lunar Sci. Conf.*, *5th*, 2703–2708.

Cull, J. P. (1978), Thermal contact resistance in transient conductivity measurements, *J. Phys. E Sci. Instrum.*, *11*, 323–326, doi:10.1088/0022-3735/11/4/014.

Cuzzi, J. N. (1972), The subsurface nature of Mercury and Mars from thermal microwave emission, Ph.D. thesis, Calif. Inst. of Technol., Pasadena, Calif.

De Vries, D. A. (1952), A nonstationary method for determining thermal conductivity of soil in situ, *Soil Sci.*, *73*, 83–90, doi:10.1097/00010694-195202000-00001.

Dul'nev, G. N. and Sigalova Z. V. (1967), Effective thermal conductivity of granular materials, *J. Eng. Phys. Thermophys.*, *13*, 670–685.

Farouki, O. T. (1981), Thermal properties of soils in cold regions, *Cold Reg. Sci. Technol.*, *5*, 67–75.

Fountain, J. A., and E. A. West (1970), Thermal conductivity of particulate basalt as a function of density in simulated lunar and Martian environments, *J. Geophys. Res.*, *75*, 4063–4069, doi:10.1029/JB075i020p04063.

Gavriliev, I. (2008), Thermal conductivity of segregated ground ice, *Permafrost Periglacial Proc.*, *19*, 333–340, doi:10.1002/ppp.628.

Gundlach, B., S. Kilias, E. Beitz, and J. Blum (2011), Micrometer-sized ice particles for planetary-science experiments I. Preparation, critical rolling friction force, and specific surface energy, *Icarus*, *214*, 717–723, doi:10.1016/j.icarus.2011.05.005.

Hardy, B. (1998), ITS-90 formulations for vapor pressure, frostpoint, temperature dewpoint temperature, and enhancement factors in the range −100 to +100°C, in *Proceedings of the Third International Symposium on Humidity and Moisture*, edited by B. Hardy, pp. 1–15, Natl. Phys. Lab., London.

Hobbs, P. V. (1974), *Ice Physics*, Oxford Univ. Press, New York.

Hobbs, P. V., and W. M. Ketcham (1969), The planar growth of ice from the pure melt, in *Physics of Ice: Proceedings of the International Symposium on Physics of Ice*, edited by N. Riehl, B. Bullemer, and H. Engelhardt, pp. 95–112, Plenum Press, New York.

Hobbs, P. V., and B. J. Mason (1964), The sintering and adhesion of ice, *Philos. Mag.*, *9*(98), 181–197, doi:10.1080/14786436408229184.

Hudson, T. L. (2009), Growth, diffusion, and loss of subsurface ice on Mars: Experiments and models, Ph.D. thesis, Calif. Inst. of Technol., Pasadena, Calif.

Hudson, T. L., O. Aharonson, and N. Schorghofer (2009), Laboratory experiments and models of diffusive emplacement of ground ice on Mars, *J. Geophys. Res.*, *114*, E01002, doi:10.1029/2008JE003149.

Jakosky, B. M. (1986), On the properties of Martian fines, *Icarus*, *66*, 117–124, doi:10.1016/0019-1035(86)90011-4.

Johansen, O. (1975), Thermal conductivity of soils, Ph.D. thesis, Univ. of Trondheim, Trondheim, Norway.

Kersten, M. S. (1949), Laboratory research for the determination of the thermal properties of soils, *Bull. 28*, final report, Univ. of Minn. Eng. Exp. Sta., U.S. Army Corps of Eng., Minneapolis, Minn.

Kluitenberg, G. J., J. M. Ham, and K. L. Bristow (1993), Error analysis of the heat pulse method for measuring soil volumetric heat capacity, *Soil Sci. Soc. Am. J.*, *57*, 1444–1451, doi:10.2136/sssaj1993.03615995005700060008x.

Kossacki, K. J., N. I. Komle, G. Kargl, and G. Steiner (1994), The influence of grain sintering on the thermal conductivity of porous ice, *Planet. Space Sci.*, *42*, 383–389, doi:10.1016/0032-0633(94)90127-9.

Lacelle, D., D. Fisher, I. D. Clark, and A. Berinstain (2008), Distinguishing between vapor- and liquid-formed ground ice in the northern Martian regolith and potential for biosignatures preserved in ice bodies, *Icarus*, *197*(2), 458–469, doi:10.1016/j.icarus.2008.05.017.

Lachenbruch, A. H., J. H. Sass, B. V. Mashall, and T. H. Moses Jr. (1982), Permafrost, heat flow, and the geothermal regime at Prudhoe Bay, Alaska, *J. Geophys. Res.*, *87*, 9301–9316, doi:10.1029/JB087iB11p09301.

Langseth, M. G., S. J. Keihm, and K. Peters (1976), Revised lunar heat-flow values, *Proc. Lunar Sci. Conf.*, *7th*, 3143–3171.

Lide, D. R. (2003), *CRC Handbook of Chemistry and Physics*, 84th ed., CRC Press, Boca Raton, Fla.

Mellon, M. T., and B. M. Jakosky (1993), Geographic variations in the thermal and diffusive stability of ground ice on Mars, *J. Geophys. Res.*, *98*(E2), 3345–3364, doi:10.1029/92JE02355.

Mellon, M. T., B. M. Jakosky, and S. E. Postawko (1997), The persistence of equatorial ground ice on Mars, *J. Geophys. Res.*, *102*(E8), 19,357–19,369, doi:10.1029/97JE01346.

Mellon, M. T., W. C. Feldman, and T. H. Prettyman (2004), The presence and stability of ground ice in the southern hemisphere of Mars, *Icarus*, *169*, 324–340, doi:10.1016/j.icarus.2003.10.022.

Mellon, M. T., et al. (2009), Ground ice at the Phoenix landing site: Stability state and origin, *J. Geophys. Res.*, *114*, E00E07, doi:10.1029/2009JE003417.

Mickley, A. S. (1951), The thermal conductivity of moist soil, *Trans. Am. Inst. Electr. Eng.*, *70*(2), 1789–1797.

Paige, D. (1992), The thermal stability of near-surface ground ice on Mars, *Nature*, *356*(6364), 43–45, doi:10.1038/356043a0.

Piqueux, S., and P. R. Christensen (2009a), A model of thermal conductivity for planetary soils: 1. Theory for unconsolidated soils, *J. Geophys. Res.*, *114*, E09005, doi:10.1029/2008JE003308.

Piqueux, S., and P. R. Christensen (2009b), A model of thermal conductivity for planetary soils: 2. Theory for cemented soils, *J. Geophys. Res.*, *114*, E09006, doi:10.1029/2008JE003309.

Presley, M. A., and P. R. Christensen (1997a), Thermal conductivity measurements of particulate materials: 1. A review, *J. Geophys. Res.*, *102*(E3), 6535–6549, doi:10.1029/96JE03302.

Presley, M. A., and P. R. Christensen (1997b), Thermal conductivity measurements of particulate materials: 2. Results, *J. Geophys. Res.*, *102*(E3), 6551–6566, doi:10.1029/96JE03303.

Presley, M. A., and P. R. Christensen (2010), Thermal conductivity measurements of particulate materials: 5. Effect of bulk density and particle shape, *J. Geophys. Res.*, *115*, E07004, doi:10.1029/2009JE003483.

Presley, M. A., and R. A. Craddock (2006), Thermal conductivity measurements of particulate materials: 3. Natural samples and mixtures of particle sizes, *J. Geophys. Res.*, *111*, E09013, doi:10.1029/2006JE002706.

Putkonen, J. (2003), Determination of frozen soil thermal properties by heated needle probe, *Permafrost Periglacial Proc.*, *14*, 343–347, doi:10.1002/ppp.465.

Putzig, N. E., and M. T. Mellon (2007), Apparent thermal inertia and the surface heterogeneity of Mars, *Icarus*, *191*, 68–94, doi:10.1016/j.icarus.2007.05.013.

Sass, J. H., A. H. Lachenbruch, and R. J. Munroe (1971), Thermal conductivity of rocks from measurements on fragments and its application to heat-flow determinations, *J. Geophys. Res.*, *76*, 3391–3401, doi:10.1029/JB076i014p03391.

Schmitt, B., S. Espinasse, R. J. A. Grim, J. M. Greenberg, and J. Klinger (1989), Laboratory studies of cometary ice analogues, *Eur. Space Agency Spec. Publ.*, *ESA SP-302*, 65–69.

Schorghofer, N. (2010), Fast numerical method for growth and retreat of subsurface ice on Mars, *Icarus*, *208*, 598–607, doi:10.1016/j.icarus.2010.03.022.

Schorghofer, N., and O. Aharonson (2005), Stability and exchange of subsurface ice on Mars, *J. Geophys. Res.*, *110*, E05003, doi:10.1029/2004JE002350.

Schotte, W. (1960), Thermal conductivity of packed beds, *Trans. Inst. Chem. Eng.*, *6*, 63–67.

Seiferlin, K., P. Ehrenfreund, J. Garry, K. Gunderson, E. Hütter, G. Kargl, A. Maturilli, and J. P. Merrisone (2008), Simulating Martian regolith in the laboratory, *Planet. Space Sci.*, *56*, 2009–2025, doi:10.1016/j.pss.2008.09.017.

Slavin, A. J., V. Arcas, C. A. Greenhalgh, E. R. Irvine, and D. B. Marshall (2002), Theoretical model for the thermal conductivity of a packed bed of solid spheroids in the presence of a static gas, with no adjustable parameters except at low pressure and temperature, *Int. J. Heat Mass Transfer*, *45*, 4151–4161, doi:10.1016/S0017-9310(02)00117-5.

Smoluchowski, M. (1910), Sur la conductibilité calorifique des corps pulverizes, *Bull. Acad. Sci. Cracovie, Ser. A*, *5*, 129–153.

Tsotsas, E., and H. Martin (1987), Thermal conductivity of packed beds: A review, *Chem. Eng. Process.*, *22*, 19–37, doi:10.1016/0255-2701(87)80025-9.

Vasavada, A. R., D. A. Paige, and S. E. Wood (1999), Near-surface temperatures on Mercury and the Moon and the stability of polar ice deposits, *Icarus*, *141*, 179–193, doi:10.1006/icar.1999.6175.

Watson, K. (1964), I. The thermal conductivity measurements of selected silicate powders in vacuum from 150°–350°K, II. An interpretation of the Moon's eclipse and lunation cooling as observed through the Earth's Atmosphere from 8–14 microns, Ph.D. thesis, 186 pp., Div. of Geol. and Planet. Sci., Calif. Inst. of Technol., Pasadena, Calif.

Wechsler, A. E., and P. E. Glaser (1965), Pressure effects on postulated lunar materials, *Icarus*, *4*, 335–352, doi:10.1016/0019-1035(65)90038-2.

Wechsler, A. E., P. E. Glaser, and J. A. Fountain (1972), Thermal properties of granulated materials, in *Thermal Characteristics of the Moon*, edited by J. W. Lucas, pp. 215–241, MIT Press, Cambridge, Mass.

Winter, D. F., and J. M. Saari (1969), A particulate thermophysical model of the lunar soil, *Astrophys. J.*, *156*, 1135–1151, doi:10.1086/150041.

Wood, S. E. (2011), A general analytic model for the thermal conductivity of loose, indurated, or icy planetary regolith, *Proc. Lunar Planet. Sci. Conf.*, *42nd*, 2795.

Zent, A. P. (2008), A historical search for habitable ice at the Phoenix landing site, *Icarus*, *196*(2), 385–408, doi:10.1016/j.icarus.2007.12.028.

Zent, A. P., M. H. Hecht, D. R. Cobos, S. E. Wood, T. L. Hudson, S. M. Milkovich, L. P. DeFlores, and M. T. Mellon (2010), Initial results from the thermal and electrical conductivity probe (TECP) on Phoenix, *J. Geophys. Res.*, *115*, E00E14, doi:10.1029/2009JE003420.

O. Aharonson, E. Carey, and S. Xu, Division of Geological and Planetary Sciences, California Institute of Technology, 1200 E. California Blvd., Pasadena, CA 91125, USA.

M. Choukroun and T. Hudson, Jet Propulsion Laboratory, California Institute of Technology, 4800 Oak Grove Dr., Pasadena, CA 91109, USA.

N. Schorghofer, Institute for Astronomy, University of Hawaii, 2680 Woodlawn Dr., Honolulu, HI 96822, USA.

M. Siegler, Department of Earth and Space Sciences, University of California, 595 Charles Young Dr. E., Box 951567, Los Angeles, CA 90095, USA. (siegler@ucla.edu)